Molecular modeling of thin-film nanocomposite membranes for reverse osmosis water desalination

Majid Shahbabaei and Tian Tang*

Department of Mechanical Engineering, University of Alberta, Edmonton, Alberta, Canada

*Corresponding author: Email: tian.tang@ualberta.ca

Abstract

The scarcity of freshwater resources is a major global challenge boomed by population and economic growth. Water desalination by reverse osmosis (RO) membrane is a promising technology to supply potable water from seawater and brackish water. The advancement of RO desalination highly depends on new membrane materials. Currently, RO technology mainly relies on polyamide thin-film composite (TFC) membranes, which suffer from several drawbacks (e.g., low water permeability, permeability-selectivity tradeoff, and low fouling resistance) that hamper their real-world applications. Nanoscale fillers with specific characteristics can be used to improve the properties of TFC membranes. Embedding nanofillers into TFC membranes using interfacial polymerization allows the creation of thin-film nanocomposite (TFNC) membranes, which has become an emerging strategy in the fabrication of high-performance membranes for advanced RO water desalination. To achieve optimal design, it is indispensable to search for reliable methods that can provide fast and accurate predictions of structural and transport properties of the TFNC membranes. However, molecular understanding of permeability-selectivity characteristics of nanofillers remains limited, partially due to the challenges of experimentally exploring microscopic behaviors of water and salt ions in confinement. Molecular modeling and simulation can fill this gap by generating molecular-level insights into the effects of nanofillers' characteristics (e.g., shape, size, surface chemistry, density) on water permeability and ion selectivity. In this review, we summarize molecular simulations of a diverse range of nanofillers including nanotubes (carbon

nanotube, boron nitride nanotube, aquaporin-mimicking nanochannel) and nanosheets (graphene, graphene oxide, boron nitride sheet, molybdenum disulfide, metal and covalent organic frameworks) for water desalination applications. These simulations reveal that water permeability and salt rejection, as the major determinatives of desalination performance of TFNC membranes, significantly depend on the size, topology, density, and chemical modifications of the nanofillers. Identifying their influences and the physicochemical processes behind, via molecular modeling, is expected to yield important insight for the fabrication and optimization of the next generation high-performance TFNC membranes for RO water desalination.

1. INTRODUCTION

Water scarcity is one of the most serious challenges on the globe. With the increase in the world population and worldwide industrialization, providing ample and safe drinking water is a big concern that calls for effective solutions. The total amount of water resources on the globe is estimated to be about 1.4 billion cubic kilometers. However, freshwater constitutes only about 2.5% of the total resources with only about 0.014% directly available to human activities [1]. Desalination is one of the best strategies for converting saline or contaminated water to potable water to meet the increasing demand. Desalination can help remove impurities (e.g., salts and dissolved solids) from seawater and brackish water to supply freshwater that meets the requirements for domestic and industrial use. In general, desalination processes can be categorized into distillation or heat-driven processes (e.g., multi-stage flashing and multiple-effect distillation), geothermal desalination, electrodeionization, ion exchange, solar desalination, and membrane-based processes [2]. The last is a process driven by an external pressure to separate water from undesired particles through semipermeable membranes. Reverse osmosis (RO), forward osmosis, nanofiltration, ultrafiltration, and microfiltration are

all developed membrane processes, which are distinguished based on the size range of the rejected species. Micro- and ultrafiltration membranes are impermeable to suspended particles and macromolecules (~10-0.01 μm), while RO and nanofiltration can remove ions of all types (~0.01-0.0001 μm) [3].

More than 65% of the conventional desalination plants use RO processes [4]. RO technology possesses advantages over thermal distillation and other types of desalination processes, including operating as a continuous process with smooth working conditions, being energy-saving and environmentally friendly [5]. It is therefore a predominant technology for water purification. The development of RO membrane technology experienced a long history in laboratory study before realizing its first significant industrial application in the 1960s [6]. RO process has since been improved largely thanks to the advancement in membrane materials as the core of the entire process. The main milestones in the development of RO desalination technology are summarized in Fig.1. Despite the discovery of the phenomenon “osmosis” in 1784 [6], it took about two centuries for RO desalination to be conceptually confirmed, in the 1950s, by utilizing symmetric cellulose acetate (CA) films [7]. Even though such films were good at rejecting NaCl, they failed to provide a sufficient amount of water flux acceptable for industrial practice. One of the milestones in the industrial application of RO membranes was the development of asymmetric CA membranes by Loeb and Sourirajan [7]. The desalination performance was highly improved, with salt rejection and water flux several times larger than any available membranes at the time. It was a breakthrough because the real application of the RO process became feasible using this membrane. Upon this discovery, CA membrane was further used in pilot-scale RO desalination process in California in the 1960s, followed by the establishment of the first RO municipal plants in Florida in the 1970s [7].

On the other hand, CA membranes have shown weaknesses when they are put into long-term use. They can only operate in a narrow pH range (between 4 and 6.5) and are susceptible to biological degradation [6]. For example, at low (< 3) or high (> 8) pH [3], the size of the pores and porosity of the CA membranes increase [8], diminishing the selectivity of ions. To overcome these shortcomings, Cadotte and Peterson [7] developed thin-film composite (TFC) membranes in the late 1970s. A TFC membrane is made of two or more polymer materials and consists of a thin selective layer formed on the surface of one or more porous support layers [9]. The extremely thin selective layer (0.1 mm or less) allows high water flux while the layered structure possesses good mechanical properties and can reject a large amount of salts. There are also possibilities for the independent selection of materials for the selective and support layers in order to optimize the performance of TFC membranes [10]. Compared with CA membranes, enhanced desalination performance and stability in a wider range of pH were obtained with the TFC membranes [2]. Nowadays, TFC membranes for RO technology are mostly produced by using interfacial polymerization (IP) [11-12], a process that grants facile fabrication of the thin selective layer. Conventional IP processes usually produce a selective layer of polyamide (PA), from m-phenylenediamine (MPD) and trimesoyl chloride (TMC), on top of the membrane support. Emerging/modified IP processes (see a recent review [13]) include constructing sacrificial interlayers on the support layer, incorporating surface coating techniques into IP, tuning reaction conditions of IP, and embedding nanoscale fillers into the PA layer.

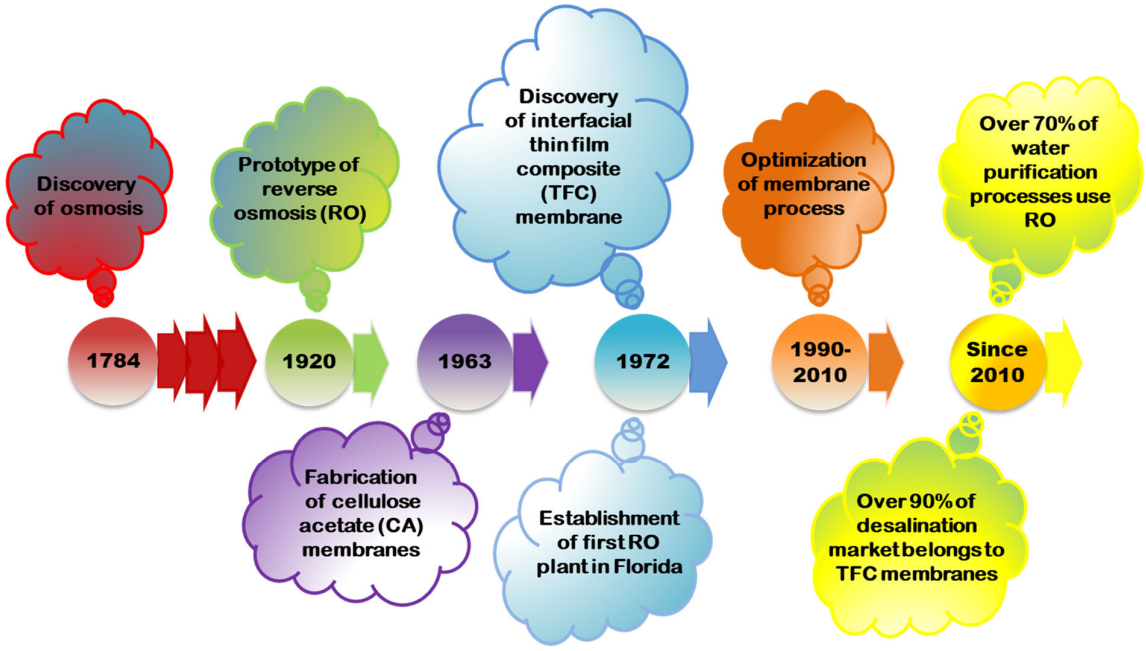

Figure 1. Historical timeline for the development of RO membranes.

Despite their improved performance, TFC membranes still face a few major challenges. They usually require high energy consumption, are prone to fouling, have a limited lifetime, and their water permeability is yet to be increased [14]. Fouling is an important phenomenon that affects the performance of TFC membranes [15]. During the desalination process, the rejected salt ions are continually accommodated on the membrane surface. The formation of a foulant layer leads to the augmentation of resistance in mass transport which reduces water flux. As a result, regular physical and chemical cleaning is required which increases the maintenance cost. Thus, there is a crucial need for exploring materials used in TFC membranes that may help reduce energy consumption while improving water permeability and antifouling characteristics.

The performance of a membrane is typically evaluated based on its permeability and selectivity. The former describes how rapidly the solvent molecules transverse a membrane, while the latter quantifies the extent to which the targeted solutes (e.g., salt ions in desalination) are

separated from other components of the feed solution. All synthetic membranes exhibit a permeability-selectivity trade-off except for highly permeable and selective biological membranes (i.e., aquaporin and ion channels) [16]. For the current TFC membranes, salt selectivity versus water permeability is constrained in the blue box in Fig. 2a, where the highest selectivity for a given permeability approaches the solid "trade-off" line [13]. An ideal membrane platform requires both high water permeability and high salt selectivity, as shown by the red-box in Fig. 2a. Yet achieving such a goal is difficult because most membrane characteristics that enhance water permeability might also induce the same effect on salt permeance [17-18], thereby decreasing the selectivity. Despite the considerable endeavors devoted to the optimization of conventional IP processes, there is still a long way (red-arrow in Fig. 2a) towards reaching the ideal membrane platform. In Fig. 2b, the selectivity-permeability relationships of TFC membranes synthesized by both conventional (blue squares) and emerging (red circles) IP processes fall below the upper bound (solid line, with numbers indicating salt ion rejection rate). Within the same range of water permeability (1 to 10 $L/m^2 \cdot h \cdot bar$), better salt selectivity is acquired by TFC membranes synthesized using conventional IP compared with emerging IP. For instance, beyond 99% rejection is achieved for most conventional IP membranes operated for seawater RO (SWRO) desalination, while the highest rejection rate obtained from emerging IP membranes is 90~99% for brackish water RO (BWRO) desalination and < 90% for nanofiltration (NF) (Fig. 2b). This is not surprising as conventional IP has been optimized for a long time to meet commercial needs, while development in emerging IP strategies is still at the laboratory scale.

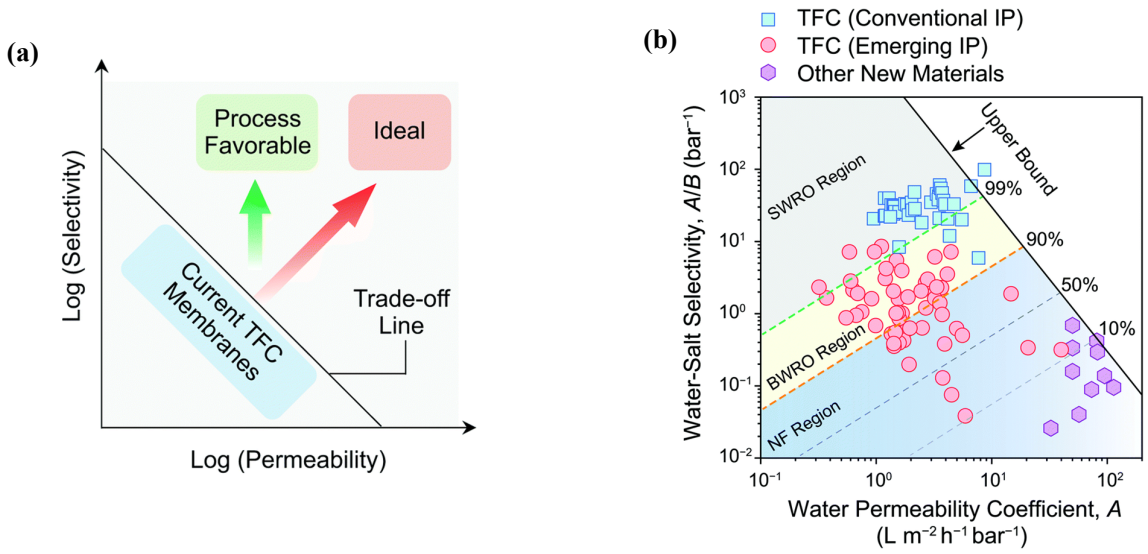

Figure 2. (a) Schematic representation of the permeability–selectivity trade-off relationship for TFC membranes, and (b) water permeability and water–salt selectivity of different types of desalination membranes. Reproduced from Ref. [13] with permission from the Royal Society of Chemistry 2021.

A few essential factors need to be considered when designing the next generation TFC membranes: proper size of the free-volume elements, a narrow free volume distribution, and a thin selective layer with tuned membrane-permeant interactions [19]. With advances in nanotechnology, high-performance and energy-efficient membranes for RO water desalination can be fabricated, for example by the embedment of functional nanomaterials (e.g., nanoscale fillers such as nanotubes and nanosheets) into TFC membranes. Embedding nanoscale fillers into the selective layer of TFC membranes enables the fabrication of thin-film nanocomposite (TFNC) membranes, which may introduce simultaneous improvements of the membrane's structural properties (e.g., surface morphology, thickness, size distribution of free volume) and surface chemistry (e.g., charge and hydrophilicity) [20]. This has the potential to offer TFNC membranes with enhanced permeability without compromising salt rejection. It is therefore a promising approach to achieve innovative designs for RO membrane desalination that overcome the existing limitations.

For over two decades, there has been considerable interest in exploring strategies for fabricating TFNC membranes [15]. Recent trends in the study of TFNC membranes are shown in Fig. 3a where the number of publications on the fabrication of TFNC membranes is gradually increasing. Initial attempts started with applying nanoparticles as fillers to provide preferential passage to desired species. Other nanofillers such as nanotubes and nanosheets have also been considered. Typically, pre-synthesized nanofillers are added into an organic phase of TMC or an aqueous solution of MPD, resulting in a PA layer with a mixed matrix structure [13] (see Fig. 3b for a schematic illustration). Such a structure may offer thermal, mechanical, and chemical stabilities in conjunction with good separation, reaction, and sorption capacities [21]. For example, using nanofillers in the form of zeolite nanoparticles, a remarkable enhancement in water permeability was obtained for the TFNC membrane compared to the bare TFC membrane, with similar solute rejections [22].

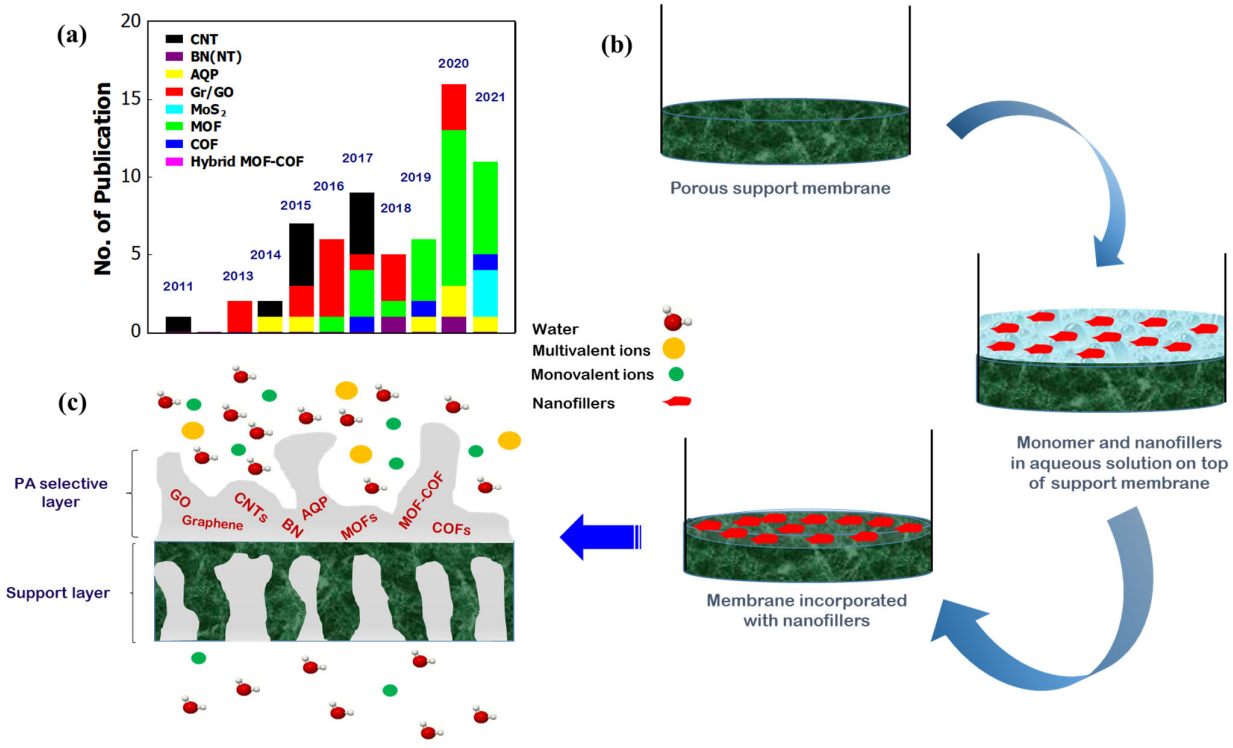

Figure 3. (a) Recent trends in the study of TFNC membranes for water treatment (2011 to 2021), with data obtained from Scopus, legend indicates different nanofillers to be discussed in Section 2; (b) schematic

presentation for the fabrication of IP-assisted TFNC membranes, and (c) an enlarged view of the selective and support layers.

Future advances in TFNC membrane technology require in-depth investigations on the material behaviors and transport properties at the molecular scale. It is extremely difficult to visualize the transport processes *in-situ* from experiments. Although some experimental techniques can provide insight into the transport capability of TFNC membranes, they cannot reveal the fine details of phenomena such as adsorption, diffusion, and solute rejection. Molecular modeling is a powerful tool that can complement experimental studies to provide a mechanistic understanding of interactions and phenomena at atomistic scale. In particular, molecular dynamics (MD) simulation is at the forefront of material design with which insights can be obtained to guide experimental processes. Since its first development, MD simulation has advanced from simulating several hundreds of atoms to systems with biological relevance [23]. Simulation of systems having 50,000-100,000 atoms is now routine, and simulations of approximately 500,000 atoms are common when appropriate computer facilities are available. MD can be performed at all-atom (AA) or coarse-grained (CG) levels, targeting different time and length scales. In an AA simulation, individual atoms are represented separately and explicitly, while several atoms are lumped into a bead in a CG simulation to reduce the computational cost. In both AA and CG MD simulations, the potential energy of the system is evaluated through a variety of bonded (bond-length, bond-angle, and dihedral) and non-bonded (Coulomb, van der Waals) interactions. The net force on each particle (a single atom in AA or a bead in CG) is calculated from the potential energy and the equations of motion are integrated to obtain its trajectory. Collectively, the motions of the particles determine the time evolution of the system. The research community involved in water desalination has used molecular simulations to address the effects of structure and chemistry of TFNC membranes on their selectivity and transport competency. These studies offer a rich knowledge of physicochemical

interactions at the membrane-nanofiller and water-ion-nanofiller interfaces, as well as fundamental mechanisms for the permeability-selectivity trade-off. This perspective review aims at providing a summary of the knowledge gathered from existing molecular modeling of TFNC membranes for water desalination, and commenting on how simulations can assist in the design of TFNC membranes.

2. Nanofillers in TFNC membranes

Typical materials used as nanofillers in TFNC membranes include zeolites, metal-organic, carbon-based materials, and bio-inspired materials [24-29]. Some examples are: carbon nanotubes (CNTs) [30], boron nitride nanotubes (BNNTs) [31], graphene [27], graphene oxide (GO) [28], molybdenum disulfide (MoS_2) [32], Metal-organic frameworks (MOFs) [33-34], Covalent organic frameworks (COFs) [35], hybrid MOF-COF [20], and aquaporin (AQP) water channels [36]. Nanofillers are diverse in their physical (e.g., size, shape) and chemical (e.g., functional group, surface charge) features [37-38]. Thus deposition of these nanomaterials into the PA layer must be carefully implemented in order to ensure permeability and selectivity of the membrane. For example, randomly oriented nanotubes provide a larger resistance for water molecules compared to an aligned structure, suggesting the importance of controlling potential blockage induced by the nanofillers. In addition, deposition of nanosheets on top of, instead of within, the PA layer could lead to superior surface chemistry of the membranes [19].

The compatibility between the PA selective layer and nanofillers must be achieved during the IP process to ensure the stability and durability of the fabricated TFNC membranes [39]. The dearth of compatibility may lead to detachment of the nanofillers from the membrane. Some functional groups such as -COOH, -OH, and $-NH_2$ have been employed to modify nanofiller

surfaces and enhance their interaction with the selective layer [37-38, 40-43]. And nanofillers modified with longer hydrophilic groups (e.g., 2-hydroxyethyl methacrylate, polyethyleneimine) have been shown to improve the characteristics of TFNC membrane in terms of wettability, anti-fouling, and water permeability [44-45].

Previous studies have found the existence of optimal sizes for nanofillers. For example, embedding long nanotubes (1-50 μm) or thick multi-layer nanosheets (~100 nm) into the PA selective layer could adversely influence the topology of the selective layer and affect its integrity [46-48]. Some reported nanofillers with their optimal sizes include: NH_2-TNT (amine-functionalized titania nanotube) with 5-25 nm in diameter [38], HNT−COOH (carboxylic acid functionalized halloysite nanotube) with an inner diameter of ~28 nm [49], aluminosilicate SWNTs with an outer diameter of 2.7nm and length of 150 nm [50], GOQD (graphene oxide quantum dot) with a thickness of 0.4−1.8 nm and diameter of 11 nm [51], and a-CN (acidified graphitic carbon nitride) with a length of ~350 nm [52].

The density of nanofillers is another important parameter that must be taken into consideration [53-54]. Applying an excessive amount of nanofillers is not recommended since it might adversely influence the integrity of the PA layer due to nanofiller agglomeration [55]. Decrease in the rejection rate from 98.1% to less than 34% was reported when the loading of nanoporous titanate was increased from 0.01 to 0.1 wt% [56]. A poor rejection rate was also reported for TFNC membranes with a high density of GO and multi-walled carbon nanotubes (MWCNTs) [39, 57], while reducing the density led to defect-free membranes with an exceptional NaCl rejection rate of 96-97%. Optimal loadings were reported for some nanofillers in TFNC membranes, including: 0.05 wt/v% of functionalized TNT dispersed in organic solution [37], 0.05 wt/v% of functionalized HNT in organic solution [58], 0.002 wt% of functionalized NH_2-

MWCNT in aqueous solution [41], 0.2 w/v% of aluminosilicate SWNTs in aqueous solution [50], 0.0053 wt/v% of GO in organic solution [59], and 0.1 wt% of bentonite nanosheets in aqueous solution [60].

2.1. Nanotubes

Nanotubes are typically employed in the form of CNTs or BNNTs. Using the IP process, CNTs were added in constructing TFNC membranes [25, 57, 61] with improved permeation-rejection capacity. A schematic illustration is given in Fig. 4 for the fabrication of CNT-assisted TFNC membranes. The hydrophobic nature of CNT and the formation of interfacial voids between the polymer chains and CNTs are responsible for high water permeation [62-63]. BNNT and CNT are similar in structure with the difference being a full replacement of carbon atoms in CNT with boron and nitrogen atoms. Using IP, a BNNT-assisted TFNC membrane was fabricated and investigated for water desalination. By adding only 0.02 wt% of BNNT into the PA selective layer, a 4-fold increase in water permeability was achieved compared to bare PA membrane, at no cost to salt rejection [64]. Formation of free volume due to the presence of BNNT in the membrane matrix provides pathways for water molecules, thereby increasing the water flux.

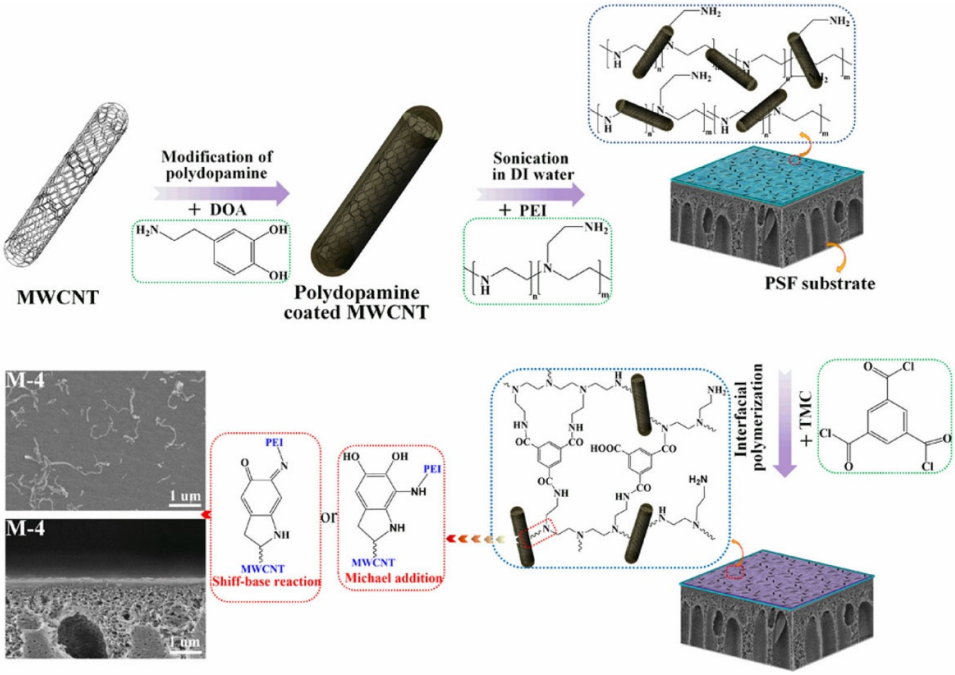

Figure 4. Preparation of TFNC membranes from polydopamine (PDA)-coated MWCNTs, polyethylenimine (PEI), and TMC via IP process. Reproduced from Ref. [63] with permission from the American Chemical Society 2016.

2.2. Nanosheets

Various two dimensional (2D) nanomaterials including BN, graphene, GO, MoS_2, MOFs, and COFs have been studied for TFNC membrane fabrication. Incorporating BN nanosheets, a novel BN-assisted TFNC membrane was fabricated, which was characterized as positively charged and highly hydrophilic. The membrane produced 59% and 50% improvement in water flux and fouling resistance, respectively, in comparison to the control counterpart [65]. GO has excited great interest in its integration into TFNC membranes thanks to its ultra-thin nature and abundant oxygen functional groups [5]. Despite improvement in water permeability and salt rejection provided by GO-assisted TFNC membranes, dispersion of GO nanosheets into the PA selective layer is challenging [66-67], which can be tackled by chemical modifications [68-70]. For TFNC membranes fabricated with sulfonated-GO (sGO) nanosheets, it was reported that the density of sGO determines the properties and performance of the membranes, including

hydrophilicity, surface roughness, charge density, water permeability, and antifouling capability. An sGO loading of 0.3 wt% showed 87.3% improvement in water permeability compared to bare TFC membrane, as well as 95% of $MgSO_4$ rejection [69].

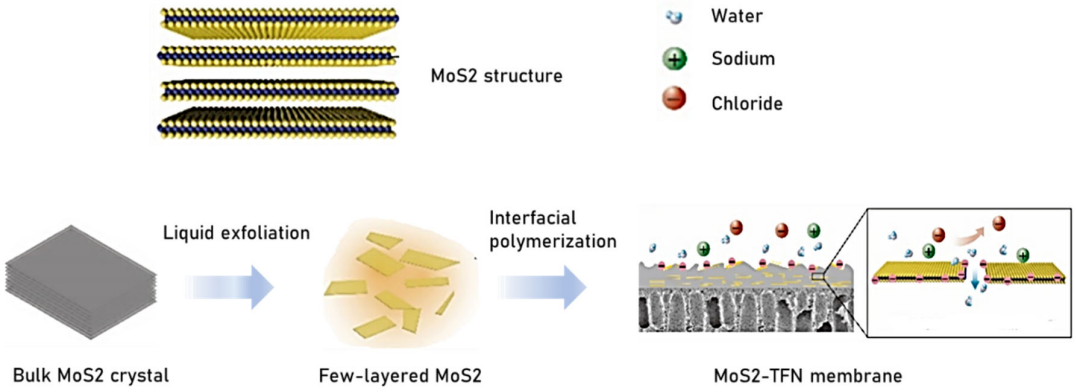

Figure 5. Schematic of TFNC membrane fabricated with MoS_2 nanosheets. Reproduced from Ref. [74] with permission from Elsevier 2019.

MoS_2 is composed of layers of molybdenum (Mo) and Sulfur (S) forming hexagonal structures [71-72]. MoS_2 is characterized as a strong, negatively charged, and hydrophilic nanomaterial that is suitable for water purification applications [73]. In general, MoS_2 nanosheets have intrinsic pores. The size of these pores are small but can be adjusted to facilitate water conduction. Salt rejection of MoS_2 pores could also be increased by engineering them with Mo- and S-terminated edges. Using IP, a multilayered MoS_2 was used to fabricate TFNC membranes for RO water desalination, as shown in Fig. 5. Compared to a bare TFC membrane, the MoS_2-assisted TFNC membrane showed increased salt rejection and higher water flux with superior fouling resistance [74].

Possessing a network porous structure with uniform nanoscale pores, MOFs are similar to water channels which speed up water permeation while blocking ions. The embedment of MOFs into the PA selective layer was reported to result in enhanced water permeability and

salt rejection efficiency [75-76]. On the other hand, the agglomeration of MOFs is a serious issue which can degrade the integrity of the PA selective layer. Via IP, Zhang et al. [77] used UiO-66-NH_2 to fabricate defect-free MOF-assisted TFNC membranes, as shown in Fig. 6a. COFs are also prominent candidates for designing molecular sieving membranes, as a class of highly crystalline porous materials with large surface area, tunable pore size and structural stability [78]. A COF-assisted TFNC membrane was fabricated on polysulfone (PSF) substrate with triformylphloroglucinol and p-phenylenediamine (TpPa) using the IP process (Fig. 6b). The membrane showed a remarkable dye rejection of 99.5% and water permeability of up to 50 $L/m^2 \cdot h \cdot bar$, which is 2 to 10 times higher than that of commercial membranes with similar ion rejection. Membranes based on MOF and COF materials should not suffer permeability-selectivity trade-offs which threaten traditional polymeric membranes [79]. The crystalline nature of MOFs and COFs means that the pores of many of these framework structures are non-deformable [80], thus selective permeability can be achieved based on the size of the particles. For example, the zeolite imidazolate framework (ZIF)-8 membrane synthesized by Gupta et al. [81] had pores of ~3.4 Å in diameter, which was effective in transporting water (~3 Å in size) while blocking alkali metal ions of larger hydrated diameter: Li^+ (7.64 Å), Na^+(7.16 Å), K^+(6.62 Å), and Rb^+(6.58 Å) [82]. As another example, functional COF-300 membrane with pore size of 7.2 Å was capable of rejecting 96% of hydrated Mg^{2+} ions (8.5 Å in diameter) [83].

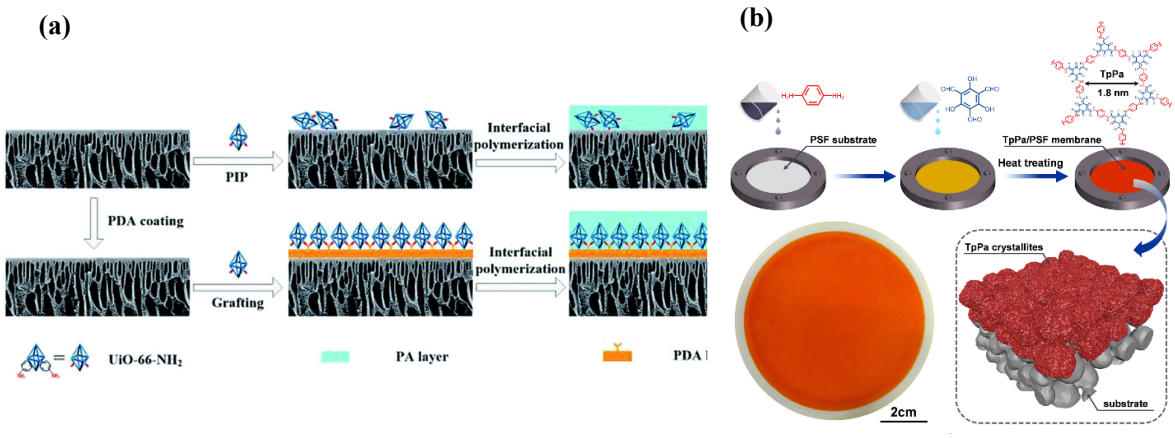

Figure 6. (a) Schematic comparing (top) evaporation-controlled filler positioning and (bottom) conventional TFNC membrane preparation with UiO-66-NH_2. Reproduced from Ref. [77] with permission from the Royal Society of Chemistry 2019. (b) Schematic representation of the fabrication process of TpPa/PSF membranes using IP. Reproduced from Ref. [78] with permission from the Elsevier 2018.

Constructing multi-component porous materials such as hybrid MOF-COF could provide a new route for the development of TFNC membranes. Crystalline MOFs consist of small repeating units in the range of a few nanometers, similar to the inner pore size of COFs. Theoretically, COF pores can be filled with unit cells of MOFs (in the form of a chain or a cage). A few works have discussed emerging strategies for fabricating hybrid MOF-COF membranes [84-88], and the schematic of an MOF-in-COF membrane is shown in Fig. 7. Fan et al. [84] demonstrated that integrated MOF-COF pore systems with ordered micro-nanochannels offered exceptional molecular sieving for gas separation. While to date hybrid MOF-COF membranes have been mainly developed for gas separation [84, 89], their generalization to liquid separation is of great potential. By combining micro and nanoscale pore networks, hybrid MOF-COF may produce high water transport rate with remarkable sieving performance suitable for RO water desalination [85].

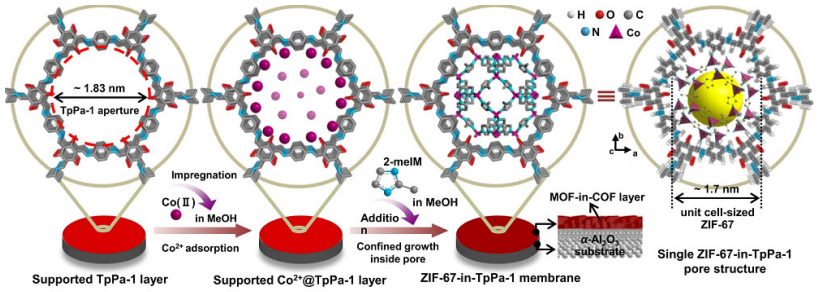

Figure 7. Schematic representation of MOF-in-COF membrane prepared using ZIF-67 MOF and TpPa-1 COF. Reproduced from Ref. [84] with permission from the Springer Nature 2021.

2.3. AQPs

AQPs are protein water channels ubiquitous in our living cells [90]. The unique hourglass-shaped structure of AQPs (Fig. 8a) enables high water permeability and good salt selectivity which is the motivation behind the recent advances in the adoption of such materials in the fabrication of artificial membranes [36, 91]. AQP-based biomimetic membranes were previously prepared by directly fusing AQP-integrated liposomes (proteoliposomes) or polymersomes onto a substrate to form a dense 'skin' layer [92-96]. Unfortunately, the membrane showed vulnerability to the external environment and poor scalability. These issues were tackled by Li et al. [36] where IP was used to prepare a highly permeable and selective hollow fiber composite membrane incorporated with AQP-Z (Fig. 8b). **Error! Bookmark not defined.**The resulting membrane showed an exceptional water flux (200% larger than a typical commercial RO membrane) and a remarkable 97.5% salt rejection (much higher than commercial membranes operating under the same condition).

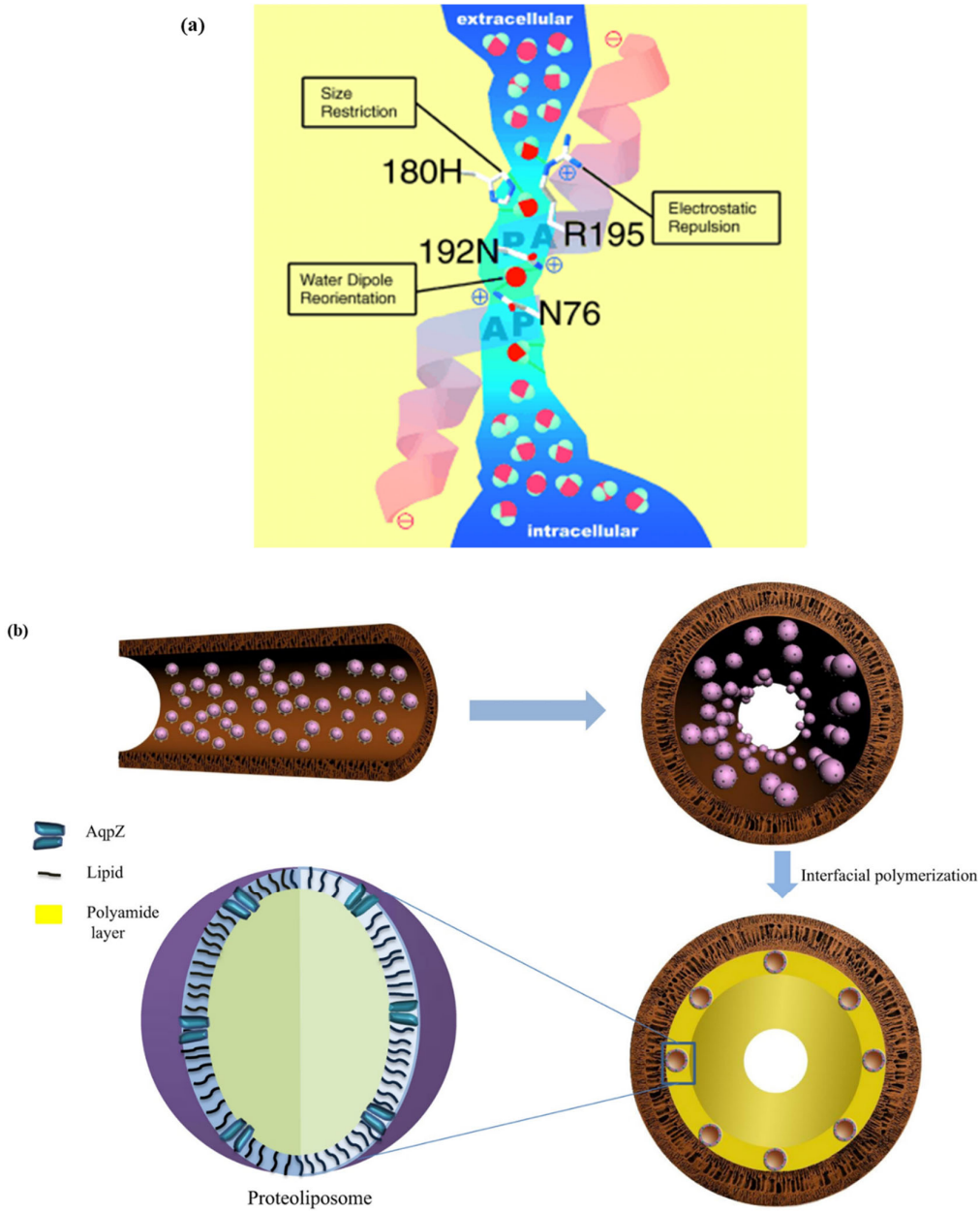

Figure 8. (a) Schematic depicting an AQP water channel. Reproduced from Ref. [90] with permission from the John Wiley and Sons 2004. (b) Preparation of AQP-based hollow fiber membrane using IP. Reproduced from Ref. [36] with permission from the Elsevier 2015.

3. Molecular modeling

3.1. Molecular dynamics simulation

MD simulations have helped to provide a valuable understanding into the architecture and functionality of membranes synthesized from different materials and/or different methods [97-98]. The fundamental principles behind AA and CG MD simulations are similar, as well as the associated numerical treatments and post-analyses. Some of the principles are summarized below.

MD requires the definition of intra- (bonded) and inter- (non-bonded) molecular interactions. A complete set of definitions along with the parameter values constitutes a force field. The bonded interactions usually include the two-body bond-stretching potential, three-body angle-bending potential, and four-body dihedral potential [99-100]. An example is given below;

$$U_{bonded} = \frac{1}{2}\sum_{bonds} k_b(r - r_0)^2 + \frac{1}{2}\sum_{angles} k_\theta(\theta - \theta_0)^2 + \frac{1}{2}\sum_{dihedrals} k_\phi(1 + \cos(n\phi - \phi_0)) \quad (1)$$

where k_b is the constant of the bond potential, r is the current bond length and r_0 is the reference bond length. In the second term, k_θ is the constant of the angle potential, θ is the current bond angle and θ_0 is the reference bond angle. k_ϕ is the constant of the dihedral potential, n is the number of minima in the dihedral potential (usually referred to as multiplicity), ϕ is the current dihedral angle, and ϕ_0 is called the phase factor. The non-bonded interactions are typically described by the Lennard-Jones (LJ) and Coulomb potentials, representing the van der Waals (vdW) and electrostatic interactions, respectively [101]:

$$U_{non-bonded} = \sum_{pairs}\left\{4\varepsilon_{ij}\left[\left(\frac{\sigma_{ij}}{R_{ij}}\right)^{12} - \left(\frac{\sigma_{ij}}{R_{ij}}\right)^{6}\right] + \frac{1}{4\pi\varepsilon_0}\frac{q_i q_j}{R_{ij}}\right\} \quad (2)$$

where R_{ij} is the separation between a pair of atoms i and j, $2^{1/6}\sigma_{ij}$ and ε_{ij} are respectively the location and depth of the LJ potential well, ε_0 is the permittivity of vacuum, and q_i and q_j are the atomic charges of atoms i and j. In the context of TFNC membrane, a number of force fields have been employed for the simulation of water-salt systems in carbon-based materials [102-105], MoS_2 [106], MOFs [107], and COFs [108], including the universal force field [109], Dreiding force field [110], and OPLS-AA force field [111].Three models are most commonly used for water: SPC/E [112], TIP3P [113] and TIP4P/2005 [114]. Comprehensive reviews of the force field development for nanoporous materials and water-salt-membrane systems can be found in [101, 115].

Both equilibrium MD (EMD) and nonequilibrium MD (NEMD) simulations can be performed to model water desalination membranes. In EMD, there is no biasing force and transport properties are determined from mean square displacements (MSD) or correlation functions based on linear response theory [116]. EMD simulations are typically used to investigate structural characteristics such as the hydration of ions in narrow pores [117]. In contrast, NEMD simulations are implemented by applying a biasing force such as pressure or concentration gradient [118-119] across the membrane. NEMD more closely mimics the real RO desalination process, in which a hydraulic pressure is applied as the driving force [120], and hence captures transport phenomena more directly.

To apply the biasing force in NEMD, diverse methods have been used such as introducing a moving piston/wall [118], applying an external force on atoms [121], and performing dual control volume grand canonical MD (DCV-GCMD) [122]. For instance, a moving piston/wall was used to study CNT [118], PA [123] and polymeric FT-30 [124] membranes for RO processes, and ZIF membranes for water desalination [125-126]. One drawback of this method

is that the length of the simulated system is restricted by the number of molecules in the feed reservoir, which is called the feed depletion problem [127]. This problem can be resolved by removing a certain amount of molecules from the permeate side and adding them to the feed solution at regular intervals [128]. By applying an external force on the water molecules, a NEMD simulation was conducted to study the transport of water across a biological membrane [121]. A similar approach was used to demonstrate water desalination through PA membranes [129]. Through the periodic boundary condition, this method ensures that molecules are circulated from the permeate side back to the feed side, thus avoiding the feed depletion problem. Care should be exercised when using this approach, as the application of an external force to the entire simulation system can result in malfunction of the thermostat or barostat [130]. Combining Monte-Carlo and MD, the DCV-GCMD approach has been used in modeling diverse membrane systems, such as porous silica membranes [131], simplified slit-like micro-pores [132], and carbon molecular sieve membranes [133]. This method is based on trial insertion/deletion of fluid molecules to/from control volumes of the feed and permeate sides of the membrane, and the trial moves are accepted or rejected according to the Monte-Carlo principle. This approach may not work efficiently for dense fluids because of the low acceptance rate of the trial insertion/deletion. Performing reliable simulations using this method also requires careful optimization on the ratio between molecule insertion and deletion [130].

3.2. MD-derived static and dynamic properties related to membrane transport

Several static and dynamic properties can be derived from MD output to assess membrane performance. Water permeability and ion selectivity are the most important quantities and they can be obtained from NEMD simulations. Water permeability can be determined by first calculating the water flux J (with a dimension of volume/(area·time)), defined as [121, 134]

$$J = \frac{V}{A\Delta t} \tag{3}$$

where V is the volume of water that crosses the membrane during Δt, and A is the area of the membrane. The permeance, l_p (volume/(area·time·pressure)) [121], is then obtained from

$$l_p = \frac{J}{\Delta P} \tag{4}$$

where ΔP is the pressure difference across the membrane. The permeability φ can be calculated by [135]

$$\varphi = l_p \delta = \frac{J\delta}{\Delta P} \tag{5}$$

where δ is the thickness of the selective layer. It should be noted that in the literature, permeance and permeability are often used interchangeably. Most data for permeability has been reported in the unit of L/m^2·h·bar, which strictly speaking is the permeance. In this review, we will respect the original data and summarize "permeability" data in the same unit.

Ion selectivity is usually characterized by the rejection R, calculated from $R = 1 - c_p/c_f$ where c_p and c_f are respectively the concentrations of ions ($\frac{\#\ ions}{\#\ water\ molecules}$) in the permeate and feed reservoirs. Since NEMD usually starts with vacuum on the permeate side, c_p can be calculated from $c_p = f_i/f_w$, where f_i and f_w are respectively the number of ions and water molecules that flow to the permeate side. Meanwhile, $c_f = n_i/n_w$, where n_i and n_w are the initial numbers of ions and water molecules in the feed side. R can therefore be written as [136]

$$R = 1 - \frac{f_i}{f_w}\frac{n_w}{n_i} \tag{6}$$

where the smaller f_i is, the closer R is to 1, corresponding to higher ion rejection and selectivity. Other definitions have also been used to calculate ion rejection, such as [137]

$$R = 1 - \frac{f_i}{n_i} \tag{7}$$

or [138]

$$R = \frac{n_{final}}{n_i} \tag{8}$$

where n_{final} is the final number of ions remaining in the feed reservoir at the end of the simulation. R evaluated from (7) and (8) can be different if there are ions trapped inside the membrane.

Two quantities often extracted from EMD trajectories are the radial distribution function (RDF) and the MSD. RDF describes the distribution of a certain group of particles (target particles) around a reference particle. Mathematically, it is a function of the distance from the reference particle and given by the ratio between the local density of the target particles and their bulk density. RDF can be used to explore the mechanisms behind the movement or blockage of ions in TFNC membranes, by assessing the structure of water molecules surrounding the ions [139]. MSD is computed via equation (9), usually for particles located in the membrane region, and can be used to quantify the mobility of particles in confinement [140].

$$MSD(t) = \frac{1}{N}\sum_{i=1}^{N} < |\mathbf{r}_i(t) - \mathbf{r}_i(0)|^2 > \tag{9}$$

Here $\mathbf{r}_i(t)$ is the position vector of particle i at time t, $\mathbf{r}_i(0)$ is the initial position of the same particle, and the average is performed over all particles of the same species in the region of interest (N is total number of such particles). Based on the Einstein relation [141], the self-diffusion coefficient (D) can be extracted from the slope of MSD vs. time curve:

$$D = \frac{1}{6}\lim_{t\to\infty}\frac{d}{dt}MSD(t) \tag{10}$$

While diffusivity can also be back-calculated from the flux through Fick's law [142-144], this is not often done in simulations.

4. MD studies on TFNC membranes

In the context of modeling TFNC membranes, AA simulation has been widely implemented, while there are only a few CG MD simulations that discussed membrane distillation across mesoscale graphene channels [145] and the structure of PA membranes created by IP [146]. Recent trends in the molecular modeling of TFNC membranes (either nanofillers alone or integrated nanofiller-membrane composites) and representative simulated systems are shown in Fig. 9. Unless otherwise specified, the studies reviewed in the following are NEMD simulations.

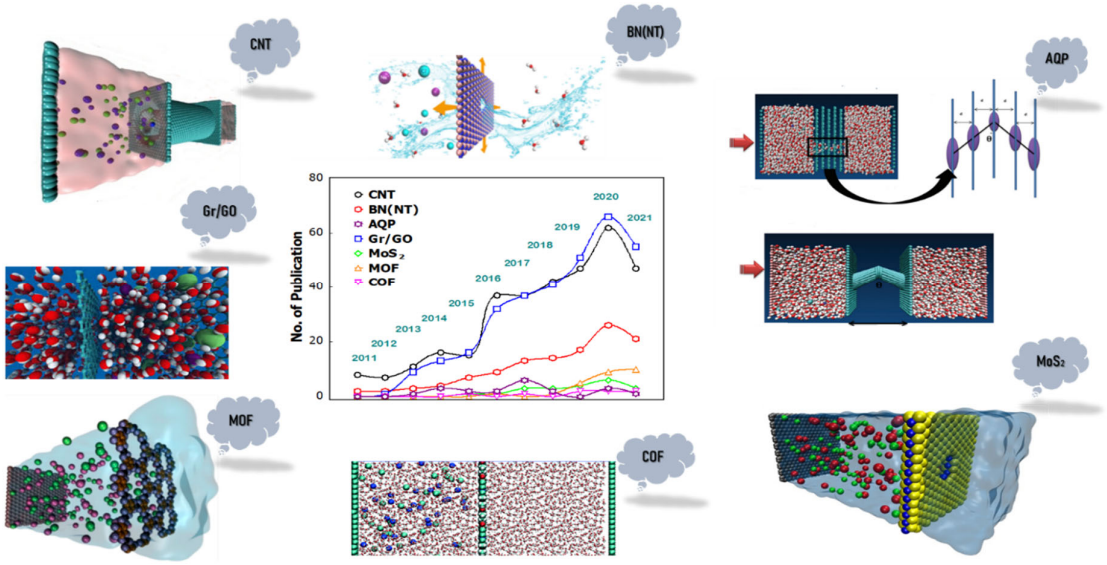

Figure 9. Number of publications on the simulation of nanofiller-based membranes for water desalination has been gradually increasing since 2011 (data from Scopus). Simulation snapshots for representative nanofillers: CNT (Reproduced from Ref. [147] with permission from the John Wiley and Sons 2020), BN (Reproduced from Ref. [148] with permission from the American Chemical Society 2017), AQP (Reproduced from Ref. [149] with permission from the Royal Society of Chemistry 2020), graphene/GO (Reproduced from Ref. [150] with permission from the American Chemical Society 2012), MoS_2 (Reproduced from Ref. [106] with permission from the Springer Nature 2015), MOF (Reproduced from Ref. [151] with permission from the American Chemical Society 2019), and COF (Reproduced from Ref. [152] with permission from the Royal Society of Chemistry 2017).

4.1. Nanotubes

The first MD simulation on water transport at the nanoscale was carried out by the pioneer group Hummer and coworkers in 2001 [102], which showed continuous and fast single-file water transport in narrow CNTs resulting from their frictionless and nonpolar interior surface. This study has inspired researchers to further investigate the potential of CNTs in RO water desalination applications. Using EMD and NEMD simulations, Corry [153] demonstrated the mechanisms of water transport and ion rejection through single-walled CNTs (SWCNTs) with different diameters. Potential mean force (PMF) analysis showed that ions experienced a large energetic barrier to pass the SWCNT with the diameter of 0.81 and 0.69 nm, while a small energy barrier was observed for wider SWCNT (0.93 and 1.09 nm in diameter). On the other hand, water molecules did not show such blockage within the SWCNTs because of the formation of tight hydrogen bonds between water molecules. Hydrogen bonding strongly influences fast water transport in CNT-assisted membranes [102], and helps maintain a continuous and smooth flow of water molecules across the CNT with low energy cost. Also in the work of Corry [153], complete (100%) salt rejection was achieved in SWCNT with an internal (considering size of C atoms) diameter of 0.47 nm, while increasing the internal diameter to 0.75 nm decreased the rejection rate to 58%. Considering different parameters including size, pressure gradient, and salt concentration, the water desalination performance of SWCNT membranes was computationally assessed by Thomas and Corry [154]. Salt rejection was found to be pressure-dependent while water permeability depended on salt concentration, with lower permeability at higher salt concentration. Simulations for different SWCNT sizes showed poor salt rejection in large SWCNTs. Ion rejection is influenced by the energy required to dehydrate the ions and enable their entrance into the CNT [153]. For larger SWCNT, fewer water molecules need to be removed for the ions, leading to a smaller dehydration barrier and

more ion permeation events. SWCNT with a diameter of ~1.1-1.2 nm showed water permeability of 22 $L/m^2 \cdot h \cdot bar$ and > 95% salt rejection (calculated via Eq. 6) [154].

The ability to enable fast water transport was computationally investigated by Suk et al. [155] for three membrane systems containing: CNT nanofiller only, BNNT nanofiller only, and polymethyl methacrylate (PMMA) with no nanofiller incorporated. MD data indicated that nanotube-based membranes produced a higher water flux in comparison to the PMMA membranes which lacked well-defined pores. Between BNNT and CNT, a higher transport rate was observed in BNNT, with a lower energy barrier at the pore entrance and in the interior. MD simulation by Won and Aluru [156] reported similar observations, where a narrow (5, 5) BNNT with a length of 1.42 nm conducted water molecules, while a CNT with the same size did not. The finding was attributed to the vdW interactions between water molecules and nitrogen atoms within BNNT which enhanced water transport. A computation endeavor reported, for (8 , 8) BNNTs functionalized with $-NH_3^+$, a complete salt rejection (100%) with a water permeability of 1250 $L/m^2.h.bar$. Strong electronic interaction between water molecules and $-NH_3^+$ groups facilitated water permeation while the space-steric effect caused by functional groups as well as the electrostatic repulsion between ions and charged functional groups led to excellent rejection [157].

Surface modification has shown to be an effective strategy to regulate the performance of nanotube-based TFNC membranes. Li et al. [158] investigated SWCNTs functionalized in the interior with different groups, $-CONH_2$, $-NH_3^+$, $-COO^-$, and -OH. It was found that the surface modification led to an exceptional increase in the water flux (about 13 times that of conventional RO membranes) across a large CNT (chirality (10, 10), length 1.35 nm). In addition, perfect rejection was achieved when the CNT was modified with four $-COO^-$ or -

$CONH_2$ groups in the interior. Surface modifications can lead to changes in pore chemistry, from hydrophilic to hydrophobic or vice versa. For example, the entire hydrophobic CNT wall became hydrophilic after -COOH functional groups were added to the interior, and the transport of a binary mixture of water and methanol was improved [159]. Different functional groups can also raise or reduce the energy barriers for the passage of cations and anions, by strengthening or weakening the electrostatic interactions between the functional groups and the ions. For instance, the attraction between $-COO^-$ groups and Na^+ was found to produce a larger energy barrier compared with the attraction between NH_3^+ and Cl^- [158].

An alternative approach for the surface modification of nanotubes is on the rims. Joseph et al. [160] demonstrated that a SWCNT (chirality (16, 16), length 1.34 nm) became highly ion-selective when its edges were modified with carboxyl and amino acid groups, while the same SWCNT without modification showed very low selectivity. The selective characteristics of the functionalized SWCNTs were also changed by adjusting the position of the functional groups on the rims. Symmetrically positioned functional groups produced greater selectivity for Cl^- ions over K^+ ions. Hong et al. [161] studied how water flux and salt rejection were influenced by charge density on the rims of (7, 7) and (9, 9) SWCNTs. Compared to uncharged ones, SWCNTs with a low charge density on the rim produced a slight increase in water flow and ion rejection, while those with a high charge density yielded a significant improvement in salt rejection (calculated via Eq. (6)) (beyond 95%) and a high water permeability of 425 $L/m^2 \cdot h \cdot bar$. While designing a new class of MWCNTs with positive and negative charges, Ghoufi and Szymczyk [147] investigated the influence of surface modification on water transport and ion rejection (Fig. 10). Fast water transport was enabled by the formation of a single-layer flow pattern in the annular region between the inner and outer walls, as well as by the presence of low friction between water and the CNT surface inside the inner tube. Modifying the CNT

surface with positive (upper surface, y>0) and negative (lower surface, y<0) charges led to the strong anchoring of water-Cl^- (for y>0) and water-Na^+ (for y<0) complexes (Fig. 10), which gave rise to clogging of the annular region while enhancing fast water transport within the inner tube [147]. The computationally designed MWCNT membrane showed superior water permeability and salt rejection compared to PA membranes and even graphene and BN nanosheet-based membranes.

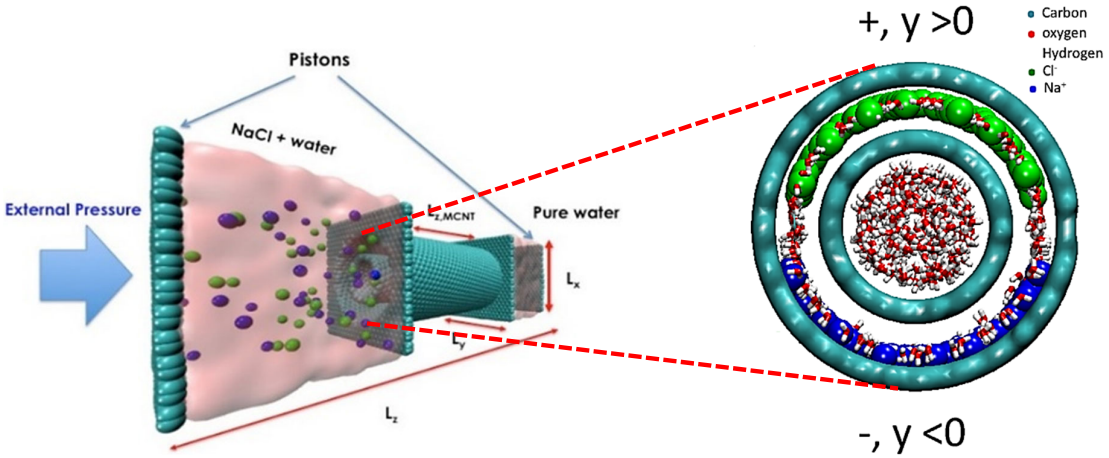

Figure 10. Schematic representation of the MWCNT membrane and the anchoring of water and ions in the annular region. The red regions correspond to water molecules. Na^+ and Cl^- ions are shown in blue (y<0) and green (y>0), respectively. Reproduced from Ref. [147] with permission from the John Wiley and Sons 2020.

An interesting strategy has been developed to create transverse flow CNTs (TFCNTs) by arranging the CNTs in a specific fashion, namely positioning multiple CNTs parallelly separated by a distance (Fig. 11(top-left)) [138, 162]. Such a design allows water conduction through the outer wall of the CNTs while impeding the larger-sized ions. MD data demonstrated that the desalination performance of this design was superior to carbon-based materials and AQP-based membranes, with permeability beyond graphene-based slit-like and commercial RO membranes [138]. The stacked CNTs form flow paths that resemble hourglass-shaped structures (Fig. 11(top-right)). According to an analytical model developed for predicting hydrodynamic resistance in tubular hourglass-shaped nanochannels [163], there is

an inverse relationship between the length of the conical channel and hydrodynamic resistance: the longer the length, the lower the hydrodynamic resistance. Thus, TFCNT membranes may provide smaller hydrodynamic resistance for water molecules in comparison to slit-like membranes. The desalination performance of TFCNT membranes strongly depends on the spacing between neighboring tubes. Exceptional salt rejection was achieved with a very small spacing of 0.228 nm and 0.328 nm (Fig. 11(bottom)) [138].

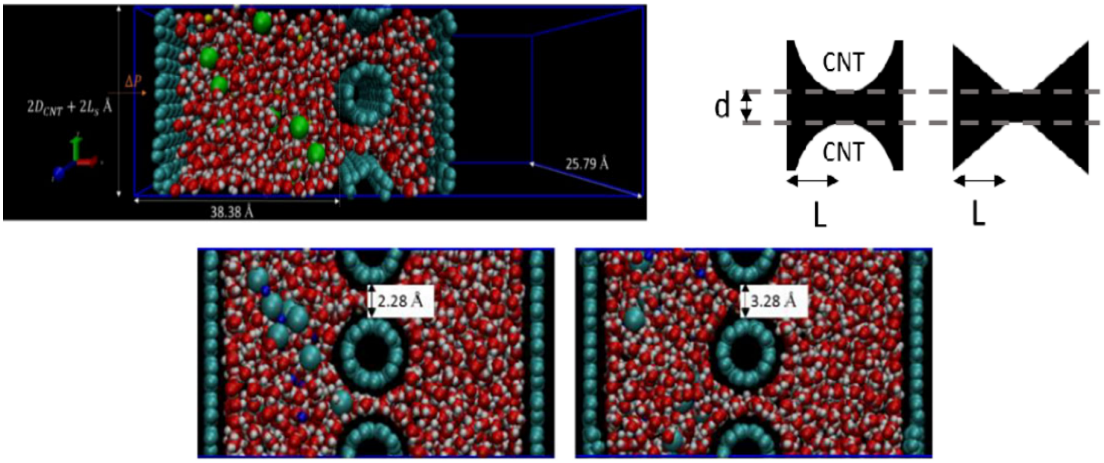

Figure 11. (Top-left) Snapshot of the simulated transverse flow CNT (TFCNT) membrane. Green and yellow spheres represent Cl^- and Na^+ ions respectively. (Top-right) Comparison between channel profile of the TFCNT membrane and hourglass shape of AQP. (Bottom) Simulation snapshots for CNT spacing of 2.28 and 3.28 Å. Reproduced from Ref. [138] with permission from the World Scientific Publishing Europe Ltd 2017.

Since the discovery of the potential application of AQP-based membranes in water desalination [119], theoretical studies have attempted to unravel the benefits of AQP-mimicking membranes. A significant effort has been devoted to understanding the mechanisms behind water transport through hourglass-shaped pores in either tubular or nanosheet structures [163-174]. These studies have provided important insights into the structure, chemistry, material, and operational conditions required for fast water transport across membranes with hourglass-shaped pores. However, to the best of our knowledge, there has been limited molecular modeling devoted to studying the ability of hourglass-shaped pores to reject salt ions [149,175-177]. MD simulation

by Razmkhah et al. [175] showed ion rejection (the method for rejection calculation was not specified) of 100%, 91.81%, 90.02% and 87.91% respectively at 50, 100, 150 and 200 MPa applied pressures for cone-shaped CNT channels, which is slightly lower than neat or hetero-junction SWCNT channels with similar entrance diameter (Fig. 12a). This result was ascribed to the entrance effect associated with the cone-shaped channel, which tended to produce smaller hydrodynamic resistance in favor of ion conductivity. The same entrance effect also acted on water, leading to remarkable water permeability. Gravelle et al. [163] reported that water flux in hourglass-shaped pores could be modulated by tuning the cone angle (the angle between cone surface and cone axis), reaching a maximum at 5º cone angle. Li et al. [176], on the other hand, demonstrated that for cone-shaped pores the optimal cone angle was 19.2° at which both high water permeability and good salt rejection were achieved, even better than graphene and MoS_2 membranes. The proposed cone-shaped membrane with an opening pore radius of 2.52 Å at the entrance acts like a molecular sieving device that rejects the passage of Na^+ and Cl^- ions, which have a larger hydrated radius of 3.58 Å and 3.32 Å, respectively. Shahbabaei and Kim [149] constructed an hourglass-shaped pore from graphene multilayers (Fig. 12b, top) as well as a tubular structure made of carbon atoms (Fig. 12b, bottom). The former structure with a bending angle of $\theta = 45º$ and the latter structure with a bending angle of $\theta = 0º$ both showed complete ion rejection (calculated via Eq. (6)). Interesting, water transport showed completely different characteristics in the two structures: frequent rupture and reformation of hydrogen bonds between water molecules within the multilayer system, while a tight single-file water arrangement within the tubular system.

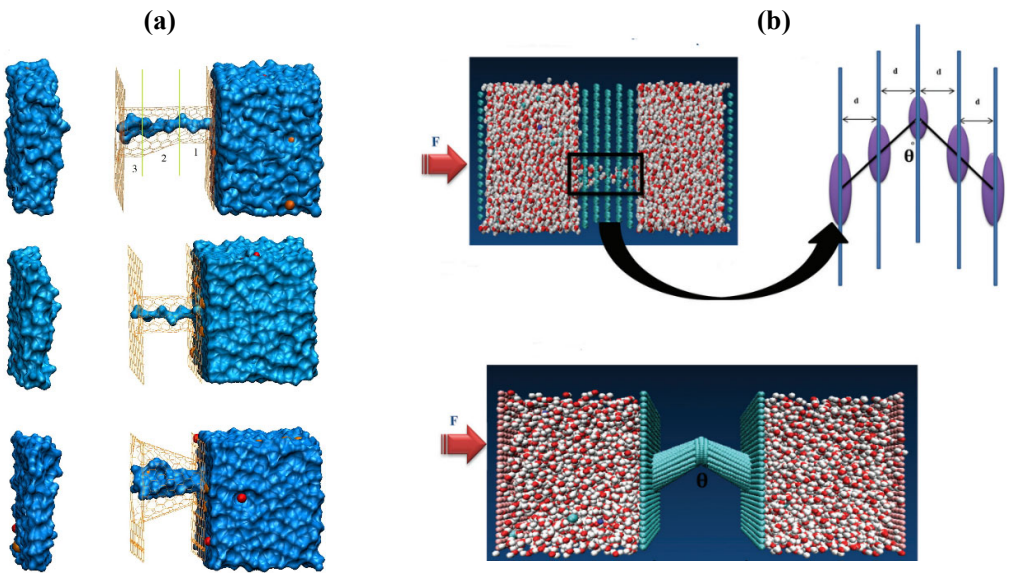

Figure 12. (a) Schematics depicting simulated systems of (top) hetero-junction CNT, (middle) neat (6, 6) CNT, and (bottom) cone-shaped CNT. Reproduced from Ref. [175] with permission from Elsevier 2016. (b) (Top-left) simulation of a membrane comprised of multilayers of graphene with layer separation *d* and an hourglass-shaped pore where the bending angle is denoted by θ, (top-right) a schematic representation of the top left figure, and (bottom) simulation of a tubular structure made of carbon atoms with a bending angle θ. Reproduced from Ref. [149] with permission from the Royal Society of Chemistry 2020.

4.2. Nanosheets

Graphene/ GO

In their pioneering work in 2012, Cohen-Tanugi and Grossman [150] computationally demonstrated the potential of graphene nanosheets for RO water desalination (Fig. 13a). Designing functionalized pores on graphene layers, they found that pores functionalized with -COOH were good at enhancing water permeability while better salt rejection was achieved through -H modification. A lower permeability-selectivity tradeoff was obtained using the modified graphene membranes compared to seawater/brackish water RO and nanofiltration membranes. Konatham et al. [178] reported that the graphene pores rejected Cl^- when decorated by $-COO^-$ and rejection of Na^+ was achieved when the pores were decorated by NH_3^+ (Fig.

13b). The finding was attributed to the large energy barrier induced by electrostatic repulsion and steric effect. MD simulation by Sint et al. [179] showed that ultra-fine (pore diameter 0.5 nm) monolayer graphene membrane can be highly selective to ions when functionalized with fluorine-nitrogen functional groups, conducting cations (Li^+, Na^+, and K^+) while rejecting anions (F^-, Cl^-, and Br^-). In contrast, graphene pore terminated with -H groups allowed the conduction of anions while blocking cations.

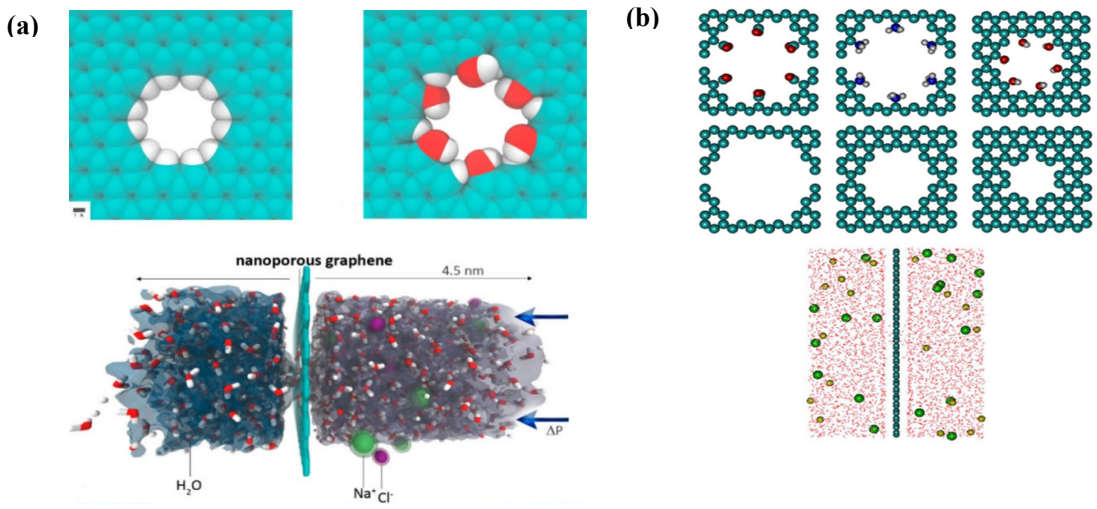

Figure 13. (a) Hydrogenated (top-left) and hydroxylated (top-right) graphene pores, and (bottom) a nanoporous graphene membrane. Reproduced from Ref. [150] with permission from the American Chemical Society 2012. (b) (Top) functionalized and the corresponding pristine pores, and (bottom) simulated nanoporous graphene membrane. Reproduced from Ref. [178] with permission from the American Chemical Society 2013.

Abundant in hydroxyl and carboxyl functional groups, GO nanosheets can be included to improve the desalination performance of TFNC membranes. The degree of oxidation is an important factor, with higher oxidation degree negatively affecting water permeability [180]. Fang et al. [181] computationally modified the edges of a GO pore via ionization. Their MD simulations showed that turning the GO pore edges from a neutral state (charge q = 0) to a moderately ionized state (q = -3e) gave rise to increased water flux, while a strongly ionized state (q = -6e) decreased water flux due to strong interactions between water and the ionized

groups. Ionization of the pore edges also increased ion rejection by reducing the size of the pore and introducing electrostatic repulsion between ions and the charged functional groups.

Pore size has a direct impact on water permeability and ion selectivity. Simulations by Cohen-Tanugi and Grossman [150] demonstrated that increasing the pore size led to increased water flux across graphene-based membranes. According to Konatham et al. [178], non-functionalized graphene with a pore diameter as large as 0.75 nm was highly ion-selective; wider pores (1.05 and 1.45 nm in diameter) lacked this feature, but the selectivity was improved by functionalization with -COOH groups. Other length scales in graphene or GO-based membranes can also influence their desalination performance. Cohen-Tanugi et al. [182] demonstrated that water flux and ion rejection across a bilayer graphene membrane strongly depended on the pore offset and layer spacing. When the interlayer spacing was smaller than 0.8 nm, bilayer with no pore offset produced high water flux and low ion rejection, while introducing an offset of 1.98 nm achieved perfect rejection at the cost of compromising water flux.

The desalination capability can be further modulated by simultaneously adjusting size and functionalization. Giri et al. [180] investigated the effect of interlayer spacing and oxidation degree on the ion selectivity of multilayer GO membranes. A GO membrane with 0.8 nm interlayer spacing and ≤10% oxidation offered the best ion sieving efficiency, along with sufficiently high water flux. Computational investigations by Hu et al. [183] and Zhao et al. [184] revealed that the passage of K^+ and Cl^- ions through a graphene pore highly depended on the pore size and pore charge density. A similar finding was reported by Kang et al. [185] where the ion size and the distance between two adjacent functional groups on the pore rim tremendously influenced the selectivity of graphene nanopores.

Molybdenum disulfide (MoS_2)

Heiranian et al. [106] assessed the desalination performance of MoS_2 membranes (Fig. 14 (top-left)) by simulating a pore in a MoS_2 monolayer terminated with Mo (effective pore size (A_p) = 56.42 Å^2), S (A_p = 57.38 Å^2), or both Mo and S atoms (A_p = 55.45 Å^2) (Fig. 15 (top-right)). The Mo-terminated pore outperformed the other models in terms of water permeability and ion rejection because of its specific pore structure resembling hourglass and fish-bone architectures, as well as its combined hydrophobic-hydrophilic characteristics (Fig. 14 (bottom)). Specifically, the Mo-terminated pore formed a geometry centrally contracted with hydrophobic S atoms while the S-terminated pore produced a centrally expanding structure (Fig. 14 (bottom)). Compared with graphene, tremendous enhancement in water flux (80% greater) and ion rejection (88%) was obtained by Mo-terminated MoS_2 membranes (the method for rejection calculation was not specified). On the other hand, the investigation by Kou et al. [186] indicated that MoS_2 membranes with mixed Mo and S sites on the pore rim and a pore size as large as 0.74 nm could perfectly reject salt ions while maintaining a water permeability beyond conventional RO membranes. In the same work, it was reported that MoS_2 membranes with an effective pore diameter of $\leq$ 0.23 nm could not conduct water, while free water conduction occurred if the pore size was greater than 0.44 nm. Enlarging the pore size beyond 1.05 nm, however, led to the complete loss of capability for the membrane to serve as a salt barrier. This study hence suggested an optimal size range for MoS_2 pores, between 0.44 nm and 1.05 nm. MD simulation by Oviroh et al. [187] revealed that tri-layer and monolayer MoS_2 membranes were effective in ion blockage and water conduction, respectively. The increase in the number of layers gave rise to better salt exclusion capacity while sacrificing water conductivity due to the increased barrier.

An interesting finding was reported by Köhler et al. [188] on the removal of heavy metal ions by MoS_2 membranes. Considering an aqueous solution containing three types of cations (Na^+, Zn^{2+}, and Fe^{3+}), the ion selectivity was found to strongly depend on the ionic charge. An excellent selectivity was achieved for trivalent Fe^{3+} cation, while the lowest selectivity was found for the monovalent Na^+. The high rejection of ferric ions was attributed to the propensity of Fe^{3+} to agglomeration near the pore, which formed long ionic chains at no expense of reducing water permeability.

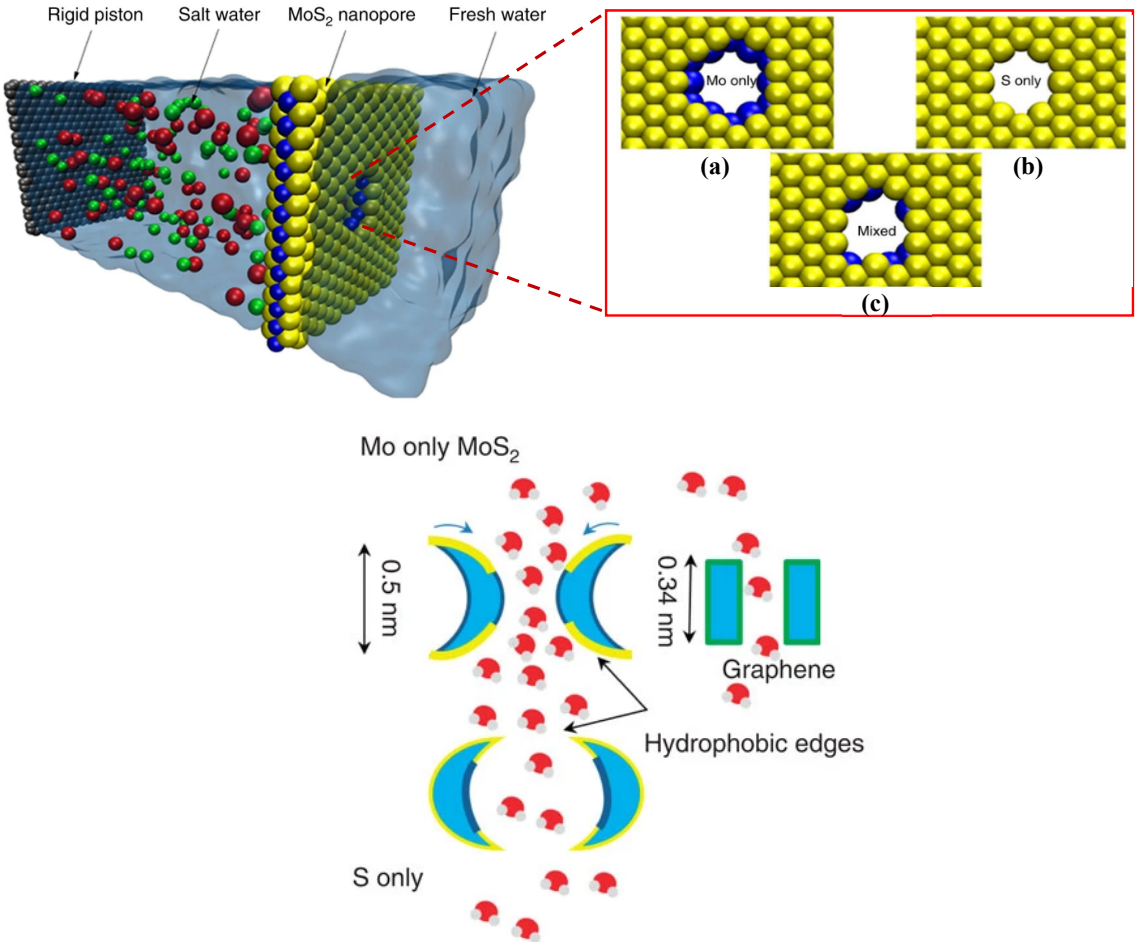

Figure 14. (Top-left) Schematic depicting a MoS_2 model membrane (Mo in blue and S in yellow). (Top-right) Pores terminated with (a) Mo only, (b) S only, and (c) mixed Mo and S atoms. (Bottom) Schematic depicting the architectures for Mo-terminated, S-terminated, and graphene pore. Reproduced from Ref. [106] with permission from Springer Nature 2015.

Metal-Organic Frameworks (MOFs)

Although microscopic understanding of gas separation via MOFs has been scrutinized, liquid separation by MOFs remains largely unexplored, and more efforts are demanded to this end [189]. The first simulation endeavor for assessing the potential of MOFs in water desalination was reported by Hu and coworkers in 2011 [125]. NEMD simulations showed that ZIF-8 nanomaterial was good at NaCl rejection due to the sieving effect of small apertures in ZIF-8, which had a size between a water molecule and hydrated ions. On the other hand, the results suggested that hydrogen bonds between water molecules were barely formed in ZIF-8 membranes due to the pore's surface interaction and topology, which negatively influenced water permeability. Although ZIF-8 showed lower water permeability in comparison to CNT or BNNT, it possesses several important characteristics that make it a good candidate for RO water desalination, at least theoretically. Strong mechanical and thermal stabilities, high pore density, and easy fabrication for small-sized pores are some advantages of ZIF-8 membranes. In contrast to biological channels which need a support layer to tolerate large pressure during RO processes, ZIF-8 nanomaterials are mechanically strong by themselves to withstand the large pressure. In addition, nanotube-based membranes are usually fabricated with low pore density (2.5×10^{11} cm^{-2}) [190], while ZIF-8 membranes can possess a much higher pore density (6×10^{13} cm^{-2}) [191]. A joint experiment-simulation effort demonstrated, for the first time, improved desalination performance of the ZIF-8 membrane grown on the polydopamin-modified ceramic support surface [192]. The reported high water flux (13.5 $kg/m^2 \cdot h$ under the pressure of 1 bar), and exceptional salt rejection (99.8%) (calculated via Eq. (7)) presented the developed ZIF-8 membrane as a promising candidate for water desalination.

Chen et al. [193] demonstrated fluorous metal-organic framework (FMOF) functionalized by CF_3 group as a new class of MOFs with adequate pore size and excellent stability in hydrated

environment. The proposed CF_3-FMOFs membrane achieved 95% salt rejection (calculated via Eq. (6)) and high water permeability of 674 L/m^2·h·bar which is orders of magnitude greater than that of commercial RO membranes (1.08~3.6 L/m^2·h·bar [22]). High water flux with 100% salt rejection was also reported for the hexaaminobenzene (HAB)-derived MOFs (Fig. 15 a (top)) in a multilayer structure. Designing HAB-MOFs with Nickel and Copper (Ni/Cu-HAB-MOFs) (Fig. 15 a (bottom)), Cao et al. [151] reported that the inherently porous structure of Ni/Cu-HAB-MOF membrane enabled water permeability that was 3~6 orders of magnitude higher than that of conventional membranes, as well as excellent ion rejection exceeding zeolite Socony Mobil-5 (ZSM-5), brackish RO, or nanofiltration membranes. Upon investigations on the interfacial diffusion near graphene and Ni/Cu-HAB MOF membranes, lateral movement of water molecules (parallel to the membrane surface) was observed near the pore entrance of the graphene membrane, while water molecules diffused in the transverse direction (perpendicular to membrane surface) near the pores of single-layer Ni/Cu-HAB MOFs (Fig. 16b). This suggested that compared with graphene, there was a lower probability for water molecules to be trapped near the surface of the MOF membrane, which resulted from the highly porous structure of MOF and its weaker interaction with water.

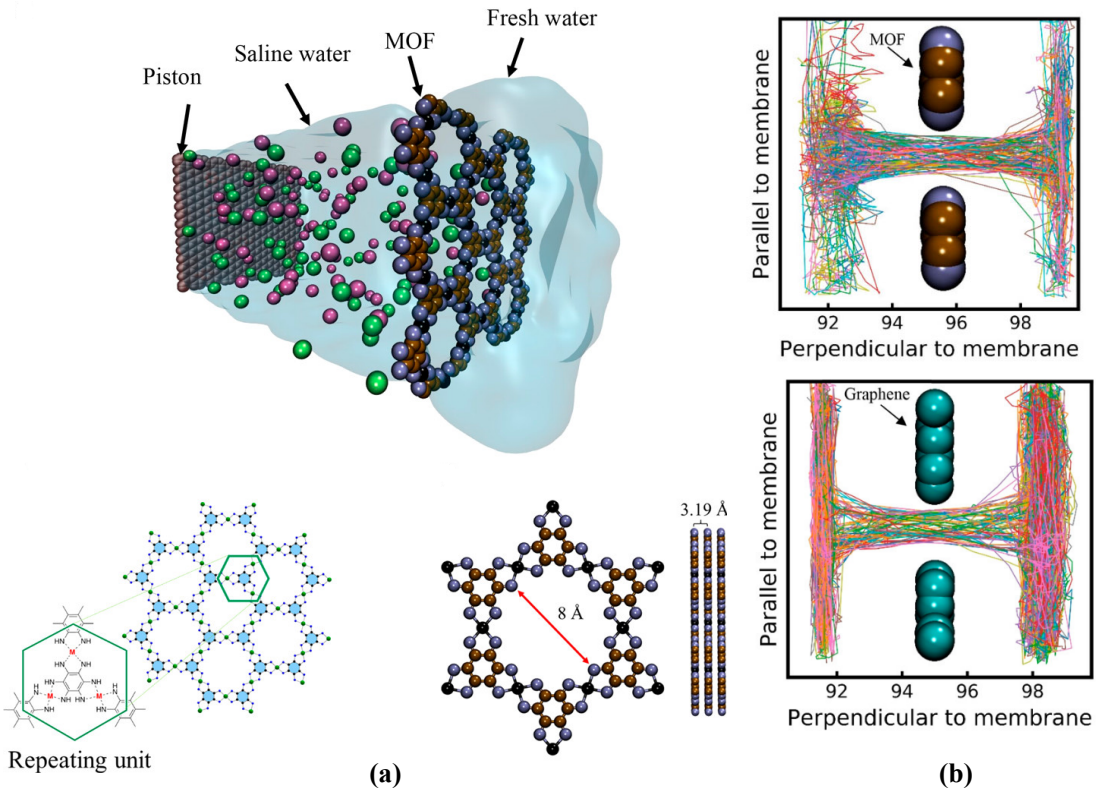

Figure 15. (a) (Top) Schematic depicting a simulation system containing a Ni/Cu-HAB-MOF membrane, a graphene piston, saline water (KCl solution), and freshwater. (Bottom-left) Chemical structure of HAB-derived 2D MOF. (Bottom-right) Detailed view of the repeating unit of a Ni/Cu-HAB MOF with pore diameter of 8 Å, and a multi-layer membrane with interlayer spacing of 3.19 Å. (b) Trajectory of water molecules near a MOF pore (top) and near a graphene pore (bottom), both under the pressure of 100 MPa. Reproduced from Ref. [151] with permission from the American Chemical Society 2019.

HKUST-1 is a class of MOFs developed by the Hong Kong University of Science and Technology (HKUST), which are widely used in gas separation applications thanks to its high permeation capacity, vast commercial availability, and easy fabrication [194]. Although HKUST-1 seems to perform well in gaseous environments [195], its potential for water desalination is limited as it is unstable in hydrated environment. Dahanayaka et al. [196] developed a hybrid membrane model by combining HKUST-1 with GO nanomaterials. The desalination performance of the HKUST-1/GO membrane evaluated from MD simulation

showed 100% salt rejection and water flux higher than that of ZIF-8 and GO membranes. It was believed that GO contributed to decreasing the water affinity of Cu atoms on HKUST-1 MOF, resulting in improvements in water permeability. However, careful control must be given to the number of GO layers added to the system as they may generate additional barriers in the molecular path.

Covalent Organic Frameworks (COFs)

Water desalination performance of a diverse series of single-layer TpPa-X COF membranes (Fig. 16(top)) with different aperture diameters (Π) and functionalities was studied by Zhang et al. [152] (Fig. 16(bottom)), including TpPa-AM2 (Π ≈0.764 nm, hydrophobic), TpPa-AMC2NH2 (Π ≈0.764 nm, hydrophilic), TpPa-OC3OH (Π ≈0.705 nm, hydrophilic), TpPa-OC4H9 (Π ≈0.686 nm, hydrophobic), TpPa-AMCOOH (Π ≈0.532 nm, hydrophilic), TpPa-OBn (Π ≈0.644 nm, hydrophobic), and TpPa-AM3 (Π ≈0.517 nm, hydrophobic). All membranes showed extremely high water permeability ranging from 1216 to 3375 $L/m^2 \cdot h \cdot bar$, which is orders of magnitude greater than that of seawater RO, brackish RO, and high-flux RO membranes. TpPa-X with larger aperture size provided larger water flux, and with similar aperture size, hydrophilic TpPa-X membranes offered higher water flux due to the preferential interaction of water with the hydrophilic walls. Excellent salt rejection (98%) was also achieved by all model membranes except for TpPa-AMCOOH which had a relatively low rejection rate of 95.8% (calculated via Eq. (7)) [152]. Zhou et al. [79] discussed water desalination through multilayered TpPa-1 COF membranes with either fully-eclipsed or offset-eclipsed alignments. Simulation data showed the presence of interfacial and interior resistances for water transport. The interior resistance, which is proportional to both inverse square of the pore radius ($1/r^2$) and the membrane thickness, originates from the breakage and formation of hydrogen bonds between water molecules and is dominated by membrane thickness (i.e.,

number of layers). The interfacial resistance, however, is subjected to the additional influence from the interaction between water and nitrogen atoms on the pore wall. It is proportional to inverse cubic of the pore radius ($1/r^3$) and independent of membrane thickness. Increasing the number of COF layers enhanced salt rejection while sacrificing water permeability (Fig. 17). The pore offset also influenced permeation and rejection, with offset-eclipsed membranes having smaller water permeability but higher salt rejection compared to fully-eclipsed membranes (Fig. 17). The offset-eclipsed membrane designed with 25 COF layers allowed complete rejection of $MgCl_2$ with water permeability beyond that of conventional nanofiltration membranes.

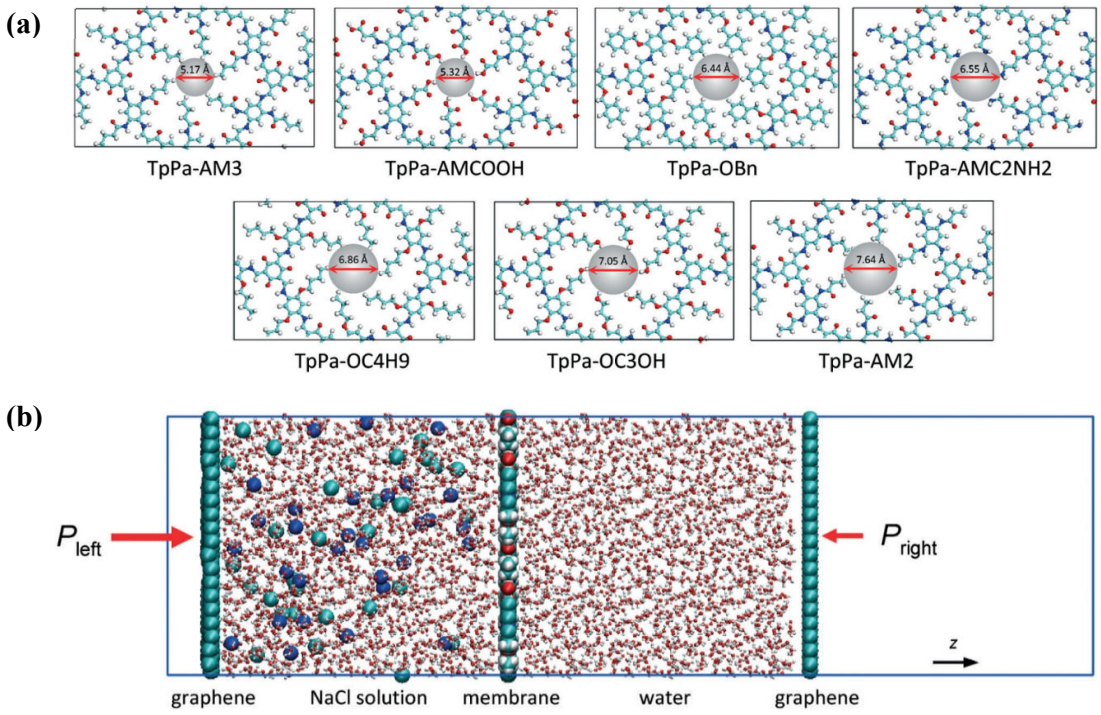

Figure 16. (a) TaPa-X structures with different pore size (Π) and functional groups. (b) Schematic depicting the NEMD simulation for desalination by TaPa-X membrane. Reproduced from Ref. [152] with permission from the Royal Society of Chemistry 2017.

Zhang et al. [197] simulated a three-dimensional hydroxyl-functionalized COF (3D-OH-COF) membrane and obtained perfect ion rejection and water permeability as high as 1727 $L/m^2 \cdot h \cdot bar$,

several orders of magnitude higher than that of commercial RO membranes and single-layer MoS_2 as calculated theoretically. The rectangular channel structure and charged hydrogens from the hydroxyl groups are responsible for the excellent desalination performance of the 3D-OH-COF membrane.

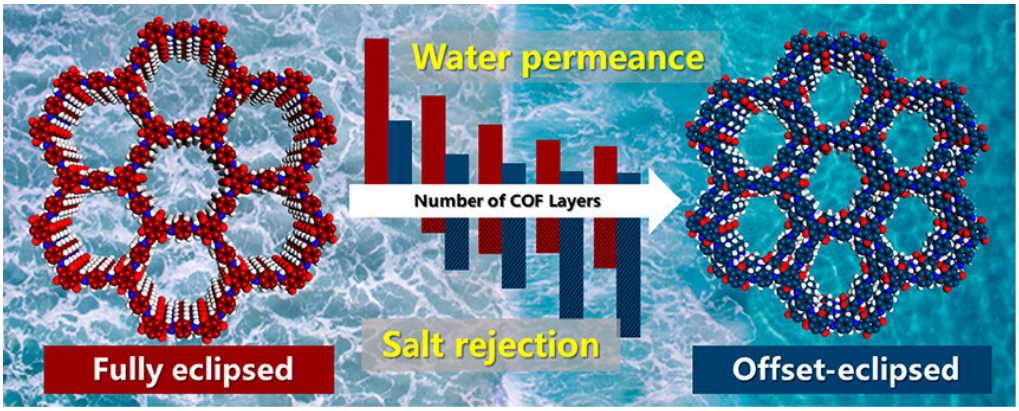

Figure 17. Schematic depicting fully eclipsed and offset eclipsed COF membranes and the trend for water permeability and salt rejection upon the increase in the number of COF layers. Reproduced from Ref. [79] with permission from the American Chemical Society 2019.

Through functionalization, COF membranes have been shown to exhibit different selectivity towards different ions. Li^+/Mg^{2+} rejection through functionalized TbPa (Triformylbenzene and p-phenylenediamine) COF membranes was reported in the computational work of Xu et al. [198]. Strong affinity of Li^+ to $-NH_2$ and Mg^{2+} to $-CH_3$ groups of the functionalized COF was demonstrated, which benefited Li^+ and Mg^{2+} rejection. Ion selectivity was also studied in multilayered membranes based on microporous phosphazene-based covalent organic framework (MPCOF) with various degrees of hydrophilicity: weakly hydrophilic (functionalized with -H, $-NO_2$, $-NH_2$, -OH groups) and strongly hydrophilic (functionalized with -COOH, $-SO_3H$, $-(NH_2)_2$, $-(OH)_2$ groups) [199]. The weakly hydrophilic membranes rejected about 50% and 95% NaCl and $MgCl_2$, respectively, while the COFs with strongly hydrophilic groups successfully rejected all ion. Both the entrance effect (hindrance induced

by pore opening) and adsorption effect (interaction between ions and pore surface) played a role in reducing $MgCl_2$ conductivity through weakly hydrophilic membranes, while the adsorption effect made a major contribution to NaCl and $MgCl_2$ rejections in the strongly hydrophilic membranes. Based on reported MD studies, when it comes to COF-assisted TFNC membranes, tailoring the number and the arrangement of the COF layers as well as pore wall hydrophilicity are important for achieving a good balance between water permeability and ion selectivity required for advanced RO water desalination.

4.3. Integrated nanofiller-matrix composites

The works reviewed in sections 4.1 and 4.2 are focused on nanofiller alone. There are also simulations that considered the integration of nanofiller and PA matrix in TFNC membranes. Araki et al. [200] implemented molecular modeling to assess the desalination performance of integrated SWCNT-PA membranes (Fig. 18a). The embedment of SWCNT into the PA film created a dense structure (hybrid SWCNT/PA membrane is 3.9% denser than bare PA) in favor of NaCl rejection. As can be seen from Fig. 18b, while Na^+ and Cl^- ions entered the membrane in absence of the SWCNT, they were completely blocked when the SWCNT was added. By adding CNTs laterally (perpendicular to flow direction) into the PA layer, the size of the pores in the membrane decreased, resulting in depressed water permeability.

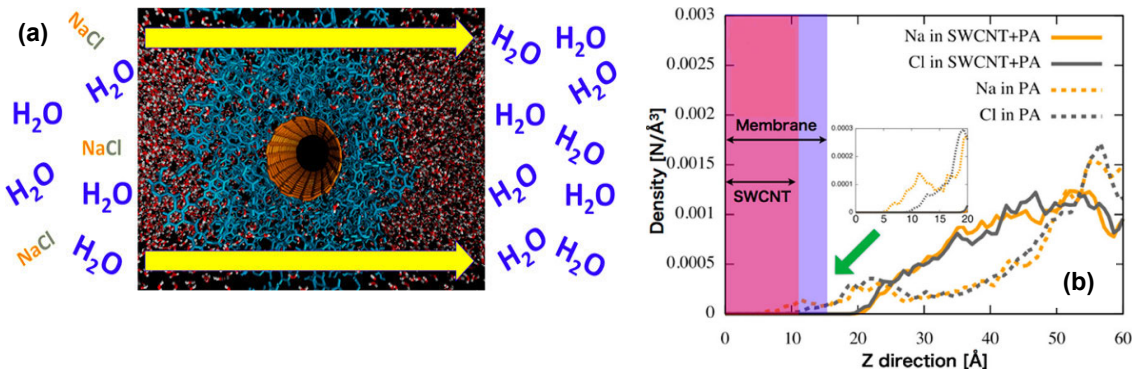

Figure 18. (a) Schematic representation of CNT/PA TFNC membrane. CNT, PA, oxygen, and hydrogen are shown in orange, indigo, red, and white respectively. The yellow arrows show the flow direction. (b) Comparison of Na^+

and Cl^- density profiles, with and without adding SWCNT. Reproduced from Ref. [200] with permission from the American Chemical Society 2015.

In another study, Araki et al. [201] discussed the mechanism of water transport across nanocomposite membranes made of CNTs and PA. CNTs were found to create hydrophilic regions within the membrane that might direct water transport by providing a lower-energy path. Gu et al. [202] demonstrated the structure and dynamics of water molecules across three atomistic membrane models: PA, PA-CNT1 (with an embedded CNT perpendicular to the membrane surface) and PA-CNT2 (with an embedded CNT parallel to the membrane surface). The addition of CNTs was found to lead to a better stacking of the surrounding PA matrix, more significantly in PA-CNT1 than in PA-CNT2, creating a denser and more rigid polymer region near the CNT. Consequently, water molecules were often guided away from the space close to the CNT. Pressure-driven water flux followed the order of PA-CNT1<PA< PA-CNT2. The more stacked PA matrix in the direction of the flow led to lower flux in PA-CNT1, while the high flux in PA-CNT2 was a result of the guiding effect as well as less severe stacking caused by the CNT. Li et al. [203] reported, through a joint experimental and MD study, high water flux across a membrane made of functionalized MWNT-$C_{14}H_{25}O_4$ and PA. The finding was attributed to the larger pore dielectric parameters, larger average pore diameter, and higher water volume fraction of the MWNT-$C_{14}H_{25}O_4$/PA membrane. Furthermore, owing to higher average charge density, ion solvation barrier and reflection coefficient, salt rejection capability of the membrane was increased by the addition of MWNT-$C_{14}H_{25}O_4$. Using experiments and MD, Fajardo-Diaz et al. [204] investigated the desalination performance of TFNC membranes where the nanofiller was a mixture of cellulose nanofiber (CNF) and multiwall CNT. Incorporating CNT and CNF simultaneously into the polyamide structure (PA-CNT/CNF) allowed homogenous dispersion of the fillers in the matrix. As a result, the hydrophobicity and surface oxygen functionalities were increased while the surface roughness was reduced

compared to bare PA, PA-CNT, and PA-CNF membranes. A salt rejection of 99.47% and a water permeability of 9.17 $L/m^2 \cdot h \cdot bar$ was experimentally achieved.

Work by Wang et al. [205] revealed, from MD simulations, that graphene/PA (Gr-PA) and graphene oxide/PA (GO-PA) composite membranes rendered higher water permeance compared to pure PA membranes. The better performance of GO/PA membrane originated from its higher water solubility. The water permeance of Gr-PA membrane was even higher, which was attributed to the lower interior transport resistance caused by the hydrophobic nature of Gr. Via experiments and modeling, Salestan et al. [206] reported water flux in a membrane made of PA incorporated with graphene quantum dots (GQDs). A higher surface wettability was found to be provided by GODs, leading to improved water diffusivity compared with bare PA membrane. In another joint experimental and MD study, Akther et al. [207] discussed the effect of GQDs on the IP reaction and membrane performance in a mixed GQD/PA/OSHF (outer-selective hollow fiber) TFNC membrane. GQDs decreased the reaction rate during the IP process by reducing the diffusivities of m-phenylenediamine and trimesoyl chloride. GQDs also reduced water permeability by acting as barriers to water molecules when present at a high concentration near the PA layer. At a very high loading, GQDs aggregated and reduced the membrane selectivity by forming non-selective voids at the interface between the PA layer and GQDs. Song et al. [208] computationally reported high water permeability in a PA/TpPa-1 composite membrane, which was 51% higher than that of the pure PA membrane. The enhancement originated from the interfacial region between COF and PA where water molecules exhibited aggregation and higher flow velocity.

5. Perspectives

Computer simulations provide substantial insights into micro- and macroscopic properties of complex materials such as TFNC membranes. The performance of TFNC membranes significantly depends on nanofillers which are diverse in topology, size, and material. Thus, it is critical to be able to understand, predict and modulate physical properties affecting the transport and sieving characteristics of nanofillers. As it is often impossible to experimentally capture the transport, adsorption and separation phenomena at the atomic scale, molecular modeling can be a complementary tool that provides unique knowledge. Most of the MD studies on TFNC membranes aim to reveal fine details related to water permeation and ion rejection characteristics of nanofillers, e.g., geometrical changes, water-nanofiller and ion-nanofiller interfaces, and transport profiles. A fundamental understanding of these characteristics may have implications for how TFNC membranes operate during real RO water desalination.

Fig. 19 (a) summarizes the MD data reported for the water flux as a function of the pressure difference across the membrane. Corresponding data for salt rejection are summarized in Fig. 19 (b). Each curve corresponds to one type of membrane, and hence there can be multiple curves from the same study. In general, as the pressure difference increases, water flux increases while salt rejection decreases. The nearly linear relationship between water flux and pressure suggests a constant water permeability in each simulated system (see Eqs. (4) and (5)). Since application of larger hydraulic pressure is associated with higher cost in RO water desalination, it is of interest to identify a few systems that exhibited good performance under low pressure. The MoS_2 pore proposed by Oviroh et al. [187] showed exceptional water flux under a small pressure difference (14~18 MPa). The simulated pore had a size of 3~6 Å in diameter, and the membrane was in either monolayer or multilayer form. The remarkable water

permeability was attributed to the enriched hydrophilic surface sites provided by molybdenum [106]. Two MOF-based membranes also exhibited good performance under moderate pressure (10 to 250 MPa): functionalized (with -CH_3) and non-functionalized single-layer FMOFs (pore diameter of 6.1 Å) [193], and double-layer HAB-MOFs functionalized with Nickle and Copper (pore diameter of 8 Å) [151]. Strong interactions between water molecules and the -CH_3 functional groups caused increased water flux in FMOF membrane. Whereas in double-layer HAB-MOFs, water molecules experienced less friction when crossing Cu-HAB pores, which led to increase in water flux. In Fig. 19 (b), the bilayer graphene membrane modeled by Cohen-Tanugi et al. [182] showed 100% salt rejection under a moderate range of pressure (50 to 200 MPa). The pores in this model were 3 Å in diameter and the interlayer space was 8 Å. The outstanding salt rejection capability was attributed to high resistance for ions to cross the membrane, which was induced by the small pore and bilayer structure. Unfortunately, the same membrane had a small water permeability (Fig. 19 (a)) and hence suffered from the permeability-selectivity tradeoff. Considering the data for both water flux and salt rejection, the FMOF-1 membrane presented by Chen et al. [193] and the bilayer Ni/Cu-HAB-MOF membrane designed by Cao et al. [151] exhibited a combination of good water permeability and salt selectivity when the pressure difference was below 100 MPa.

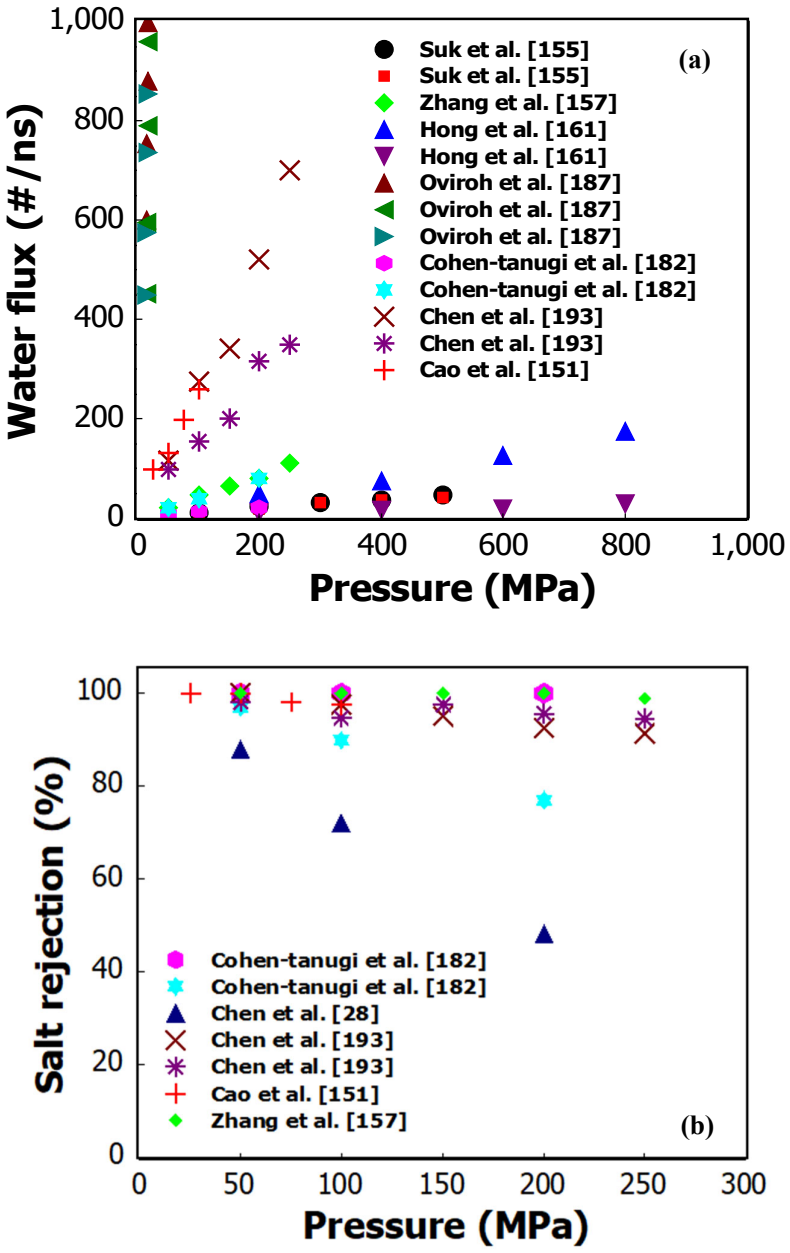

Figure 19. (a) Water flux and (b) salt rejection as functions of pressure difference across the membrane. Legend indicates the source of data. Note: as indicated earlier, different equations might have been applied in different works for ion rejection calculation. Here the originally reported data are used without modification.

From the studies reviewed earlier, it is evident that chemical modification of the nanofillers plays an important role in the performance of TFNC membranes. Li et al. [158] presented a

comprehensive molecular modeling of functionalized CNT membranes, and the results are summarized in Fig. 20. The membrane contained four CNTs each having a pore size of 10.15 Å in diameter. The CNTs were functionalized with $-COO^-$, $-NH_3^+$, $-CONH_2$, or $-OH^-$ groups. Regardless of the type of chemical modification, increasing the number of functional groups tended to reduce the water flux (Fig. 20(a)) as well as the passage of salt ions (Fig. 20(b)). The only exceptions were $-COO^-$ groups grafted to both interior and entrance of the CNTs, which showed a slight increase in water flux when the number of functional groups increased from 2 to 4, and $-CONH_2$ groups grafted to the interior of the CNTs, which showed a non-monotonic trend for the NaCl flux. The case of CNT functionalized with one $-CONH_2$ group in the interior is particularly interesting: it had a high water flux and a low NaCl flux, thus serving as a good candidate for overcoming the permeability-selectivity tradeoff. The presence of large pores (10.49 Å in diameter) in this membrane was responsible for achieving high water permeability, whereas the combination of positive nitrogen and negative oxygen in the $-CONH_2$ groups contributed to the rejection of charged ions. The type, density and placement of functional groups can hence be modulated to optimize the performance of TFNC membranes, which can be facilitated by advanced synthesis methodologies [209-211]. Of particular note, incorporating hydrophilic-rich nanomaterials into the PA layer, such as the Zinc oxide (ZnO) family including nanorods (R-ZnO), nanoflowers (F-ZnO) and nanospheres (S-ZnO), has been shown experimentally to improve the desalination performance [212]. Among them, the integrated S-ZnO/TFC membrane provided the highest water flux with good salt rejection [213]. Similarly, the incorporation of carbon quantum dots (CQD) with Na functional group into the PA layer has resulted in increased hydrophilicity with which better water permeability was obtained when desalting brackish water [214].

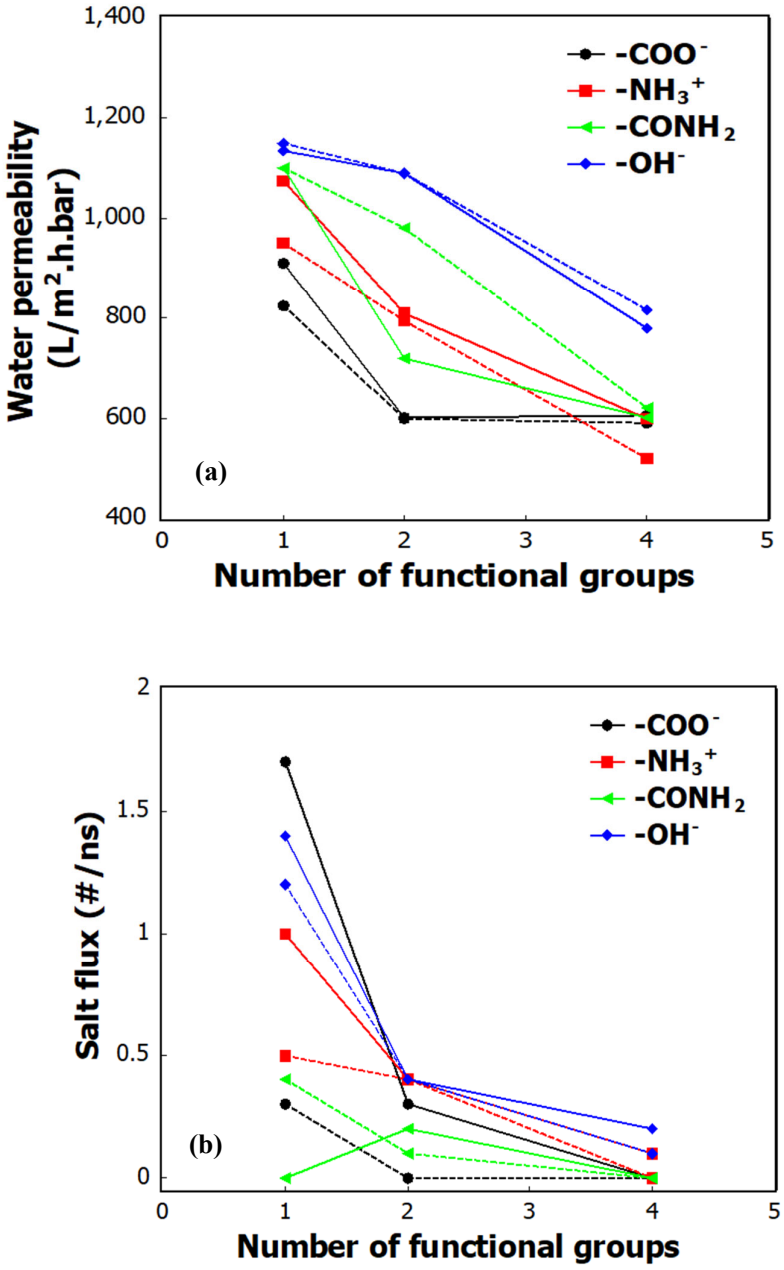

Figure 20. (a) Water permeability and (b) NaCl flux as functions of the number of functional groups grafted to the CNTs. The functional groups were either added to the interior of the CNTs (solid line), or to both the interior and the entrance (dashed line). Data from Li et al. [158].

Fig. 21 summarizes the data reported for the effect of pore size on the performance of model TFNC membranes. Overall, pore size correlates positively with water permeability, and

negatively with salt rejection. However, for some simulated systems, the relationship is not simply monotonic, for example, in Zhang et al. [152] (Fig. 21(a)) and Xu et al. [198] (Fig. 21(a) and (b)). The reason for such an observation is the coupled effect of pore size and functionalization, since chemical modification of the pore edges can simultaneously influence the size of the pore and its interaction with water and ions. Among the data summarized here, TpPa COFs pores studied by Zhang et al. [152] outperform the other systems, with much higher water permeability and nearly 100% salt rejection (calculated via Eq. (7)). Of particular note, the hydrophobic TpPa-AM_3 (diameter 5.17 Å) and the hydrophilic TpPa-OC_3OH (diameter 7.05 Å) showed comparable ion rejection, 100% and 99.5% respectively. This suggests that ion rejection through COF pores does not necessarily have a simple dependence on pore size or hydrophobicity. Although the TpPa-OC_3OH pores were large and hence poor at ion sieving, the attractive interaction between water and -OH groups facilitated the adsorption of hydrated ions, leading to exceptional performance.

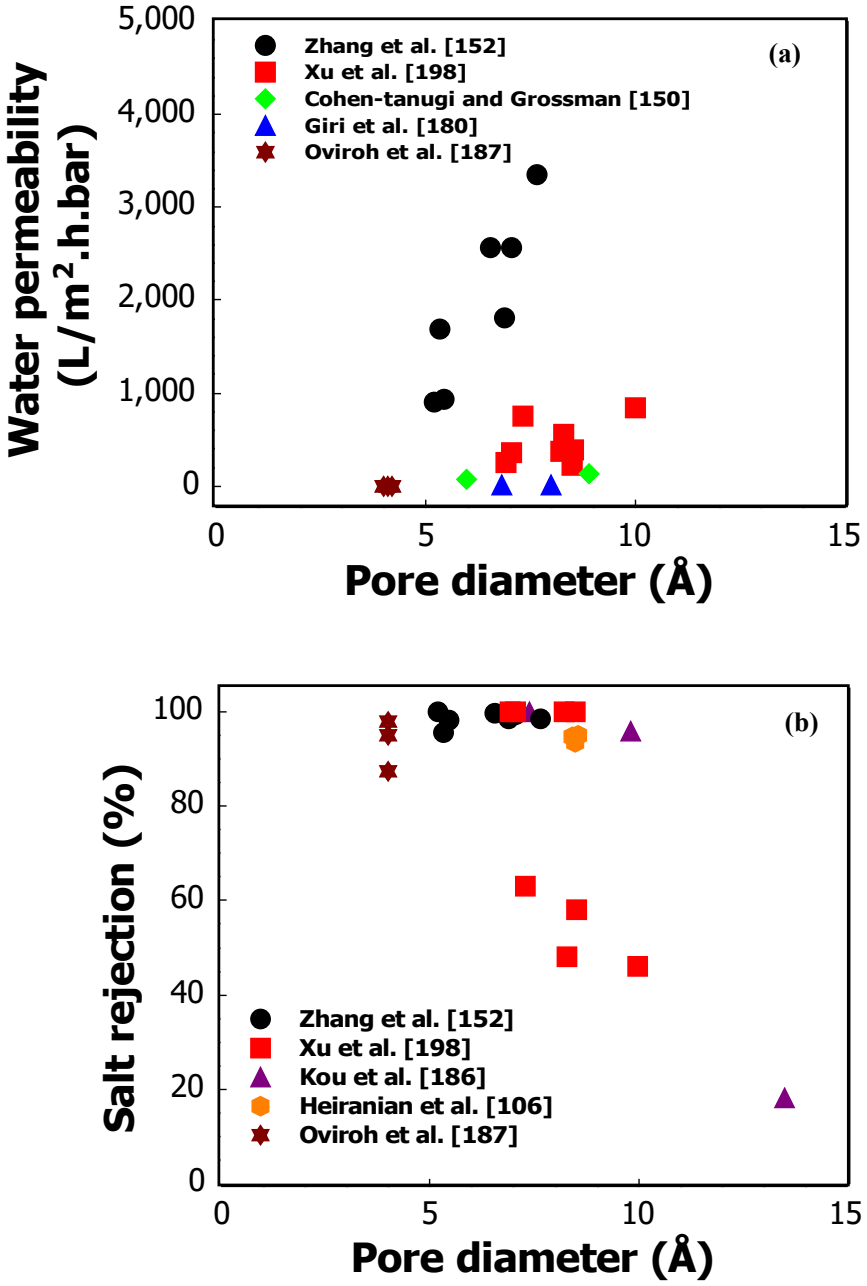

Figure 21. (a) Water permeability and (b) Salt rejection as functions of pore diameter. Legend indicates the source of data. Note: as indicated earlier, different equations might have been applied in different works for salt rejection calculation. Here the originally reported data are used without modification.

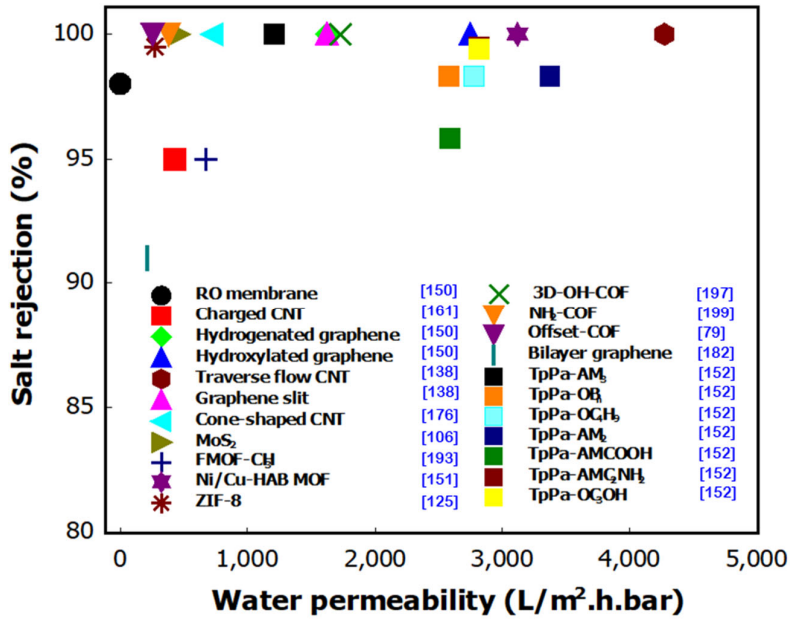

Figure 22. Desalination performance (in terms of water permeability and ion rejection) of representative TFNC membranes from simulation studies reviewed in this work. Data for RO membrane is added for comparison. Note: as indicated earlier, different equations might have been applied in different works for salt rejection calculation. Here the originally reported data are used without modification.

In Fig. 22, the water permeability and salt rejection of representative TFNC membranes from simulation studies reviewed in this work are plotted against each other. These membranes are chosen because they have shown remarkable permeability-selectivity performance. The data of RO membranes is also included for comparison. Most of the TFNC membranes exhibit higher water permeability than commercial RO membranes and comparable salt rejection. Except for a few cases (large charged CNT [161], FMOF-CH_3 [193] and bilayer graphene [182]), 100% salt rejection is achieved and the difference among them lies in the water permeability. A few strategies for improving water permeability can be drawn from this comparison: (1) increasing the size of pores or nanochannels (Hong et al. [161], Cohen-Tanugi and Grossman [150], Cohen-Tanugi et al. [182], Ang et al. [138], Li et al. [176]), (2) increasing hydrophilicity through functionalization (Cohen-Tanugi and Grossman [150], Xu et al. [199],

Heiranian et al. [106], Cao et al. [151]), (3) reducing the number of layers in 2D nanomaterial-based membranes and aligning the pores (Cohen-Tanugi et al. [182], Zhou et al. [79]), and (4) arranging nanofillers with specific structures, e.g., transverse flow (Ang et al. [138]). The exceptional behavior of TFCNT membrane could propose a new design for efficient RO technology. From studies reviewed in this work, strategies proposed to improve the ion rejection capacity of nanofiller-assisted TFNC membranes include decreasing the pore/nanochannel size, functionalization with -H, $-COO^-$, $-NH_3^+$, and $-CONH_2$ groups, modulating surface charge distribution, and for 2D nanomaterials increasing the number of layers and adjusting interlayer spacing and offset. Clearly some of the strategies to enhance permeability contradict those that improve ion rejection, so iterative optimization is often required.

As a future perspective, one understudied area in the development of TFNC membranes is AQP-like pores. It is not fully understood how the permeability-selectivity characteristics of AQP-mimicking pores are influenced by material selection, functionalization and geometry. Identifying these is expected to yield important insights for the design of hourglass-shaped nanofillers. For example, hourglass-shaped nanofillers studied so far have been limited to carbon atoms as the main structural element. It is of interest to examine other materials such as BN. The combined advantage of the topology of an hourglass-shaped channel and the proven potential of BNNT in fast water transport might offer a new, efficient nanofiller. Other types of potent nanofillers (e.g., organic, bio-based) and bioinspired polymer matrices (e.g., PDA) can also be explored. Recognizing that the discovery of novel materials through experiments can be extremely costly and time-consuming, molecular modeling provides an alternative approach in this endeavor. With advances in deep learning algorithms, artificial intelligence and machine learning approaches can be used to analyze data from experiments and molecular

modeling, and develop data-based models to predict material performance and optimize the design. Such approaches have been adopted for water-energy applications [215-216], and are expected to receive attention in the development of TFNC membranes in the near future.

While the study of nanofillers for manufacturing TFNC membranes has strongly focused on water permeability and salt rejection, the antifouling property of the membrane cannot be overlooked. Resistance against rejected salt as well as bacterial growth is important to reducing the maintenance cost and lengthening the service life of the membranes. Molecular modeling can potentially assist in the study of fouling by simulating the adsorption of salt and bacterial functional groups on the membrane, and investigating strategies for foulant removal (e.g., simple washing, heating, pH modulation or application of chemicals).

Extending lab-scale study on TFNC membranes to industrial scale requires the additional consideration of performing economic analyses, to evaluate if the new techniques are economically viable in comparison to existing commercial TFC membranes. Wasting nanomaterials during the IP process is unavoidable. For instance, MOF nanomaterials are expensive, and it remains a challenge to minimize material loss and/or enable their reuse/recycling. Other barriers also exist that hinder the upscaling and commercialization of TFNC membranes. Here, we point out a few exciting recent developments that aimed at overcoming the major barriers to TFNC membrane commercialization. A few manufacturing companies have attempted to produce commercial membranes for RO processes such as LG Chem, DOW Filmtec, and Toray [19]. Among them, NanoH_2O membranes manufactured by LG Chem using green nanotechnology showed the highest water permeability and similar NaCl rejection, compared with the membranes manufactured by DOW Filmtec and Toray. This technology utilizes bio-based natural clinoptilolite zeolite [217] and CQDs nanomaterials [218],

and its advantages include being economical, easy to fabricate and scale up [19]. Concerning RO as an expensive process requiring high hydraulic pressure to push water through dense membranes, alternative approaches have been proposed to replace the application of pressure. Gupta and Jiang [107] assessed the desalination performance of ZIF-25 model membranes induced by electro-osmosis and thermo-osmosis. In the electro-osmosis process and under an electric field of 1.5 V/nm, a water flux of 2.8×10^4 kg/m^2·h was obtained which corresponded to the application of $\Delta P = 40$ bar in pressure-induced RO process. However, salt rejection was rather poor (50%). In thermo-osmosis with a temperature difference of $\Delta T=20$ K between the permeate and feed sides, a water flux of 5.7×10^4 kg/m^2·h was achieved which was equivalent to the application of $\Delta P = 80$ bar in pressure-driven RO. The salt rejection rate was also commendable, at 98%. Various advanced techniques have been pursued to deposit nanofillers into the PA layer, including IP-based methods (ultrasound-assisted IP, filtration IP, spin-assisted IP, and electrospray-assisted IP) and surface coating (through layer-by-layer assembly, self-assembly, adsorption-reduction, and chemical interaction) [19]. Among those, the electrospray method has demonstrated high capability in the fabrication of TFNC membranes [218]. For example, this technology was used to produce a PA layer with controllable thickness ranging from 4 nm to several tens of nanometers [219]. The fabricated TFNC membranes showed increased water flux (4 times higher than that of conventional TFC membranes) [220-221] as a result of the ultrathin PA layer which is difficult to obtain by conventional IP techniques. Because of the versality of molecular modeling in capturing equilibrium and non-equilibrium states of a system, it can be used in the future to provide understanding and design principles for these newly developed manufacturing methods and processes. However, it should be recognized that molecular modeling is limited in the time and length scales that can be simulated with the current computing power and algorithms. Even experimental studies on TFNC membranes have largely focused on small samples with area on the order of cm^2 [222-

223]. Future research is required to address the fabrication and evaluation of TFNC membranes at large scale, in order to realize their potential for commercialization.

6. Conclusion

Conventional thin-film composite (TFC) membranes used for reverse osmosis water desalination suffer from fouling and permeability-selectivity tradeoff, leading to deterioration of the membrane performance during the operation time. Embedment of functionalized nanoscale fillers into TFC membranes opens the opportunity of fabricating high-performance thin-film nanocomposite (TFNC) membranes. The development of TFNC membranes requires attention to the molecular-level understanding of mechanisms underlying the transport and selectivity features of nanofillers, which are inaccessible by experiments alone. Molecular modeling is a valuable tool that can provide unique insights into the structural and functional characteristics of nanofillers in aqueous environment.

This perspective review aims to summarize molecular dynamics (MD) simulations that represent recent trend in the study and development of TFNC membranes. MD data on water permeability and salt rejection across diverse nanofiller-based model membranes have shown superior performance of TFNC membranes compared with conventional TFC membranes. The desalination capability of TFNC membranes can be modulated by properly controlling the nanofiller characteristics such as material, pore size, topology, density and chemistry. A few TFNC models with outstanding water permeability and salt rejection are highlighted. It is expected that the fundamental mechanisms behind the high performance of TFNC membranes, revealed by molecular modeling, can guide future design and fabrication of TFNC membranes for advanced RO water desalination.

Conflicts of interest

There are no conflicts of interest to declare.

Acknowledgment

TT acknowledges financial support from the Natural Sciences and Engineering Research Council of Canada (NSERC; Grant numbers: RGPIN-2018-04281, RGPAS-2018-522655), the Canada Research Chairs Program, and the Faculty of Engineering at the University of Alberta.

Bibliography

1. S. Al-kharabsheh, D.Y. Goswami. Theoretical analysis of a water desalination system using low grade solar heat. J Solar Energy Eng Trans ASME 2004, 126, 774-780.
2. M. Elimelech, W.A. Phillip. The future of seawater desalination: energy, technology, and the environment. Science 2011, 333 (6043), 712-717.
3. Y. Liu, Z. Zhang, S. Wang. Carbon Nanopore-Tailored Reverse Osmotic Water Desalination. ACS ES&T Water 2021,1, 34-47.
4. R. García-Pacheco, J. Landaburu-Aguirre, P. Terrero-Rodríguez, E. Campos, F. Molina-Serrano, J. Rabadán, D. Zarzo, E. García-Calvo. Validation of recycled membranes for treating brackish water at pilot scale. Desalination 2018, 433, 199-208.
5. Q. Liu, G.-R. Xu. Graphene oxide (GO) as functional material in tailoring polyamide thin film composite (PA-TFC) reverse osmosis (RO) membranes. Desalination 2016, 394, 162-175.
6. A.G. Fane, R. Wang, Y. Jia. Membrane Technology: Past, Present and Future, Edited by L.K. Wang, J.P. Chen, Y.-T. Hung, N.K. Shammas. Handbook of Environmental Engineering: Membrane and Desalination Technologies, Springer, New York, volume 13, 2011.
7. J. Glater. The early history of reverse osmosis membrane development. Desalination 1998,117, 297-309.

8. J.-H. Choi, K. Fukushi, K. Yamamoto. A submerged nanofiltration membrane bioreactor for domestic wastewater treatment: the performance of cellulose acetate nanofiltration membranes for long-term operation. Sep. Purif. Technol. 2007, 52, 470-477.
9. B. H. Jeong, E. M. V. Hoek, Y. S. Yan, A. Subramani, X. F. Huang, G. Hurwitz, A. K. Ghosh, A. Jawor. Interfacial polymerization of thin film nanocomposites: a new concept for reverse osmosis membranes. J. Membr. Sci. 2007, 294, 1-7.
10. A.P. Rao, N.V. Desai, R. Rangarajan. Interfacially synthesized thin film composite RO membranes for seawater desalination. J. Membr. Sci. 1997, 124, 263-272.
11. J. E. Cadotte, R. J. Petersen, R.E. Larson, E.E. Erickson. New thin-film composite seawater reverse-osmosis membrane. Desalination 1980, 32, 25-31.
12. J. Cadotte, R. Forester, M. Kim, R. Petersen, T. Stocker. Nanofiltration membranes broaden the use of membrane separation technology. Desalination 1988, 70, 77-88.
13. X. Lu, M. Elimelech. Fabrication of desalination membranes by interfacial polymerization: history, current efforts, and future directions. Chem. Soc. Rev. 2021, 50, 6290.
14. J. R. Werber, C.O. Osuji, M. Elimelech. Materials for nextgeneration desalination and water purification membranes. Nat. Rev. Mater. 2016, 1, 16018.
15. R. Zhang, Y. Liu, M. He, Y. Su, X. Zhao, M. Elimelech, Z. Jiang. Antifouling membranes for sustainable water purification: strategies and mechanisms. Chem. Soc. Rev. 2016, 45, 5888–5924.
16. H.B. Park, J. Kamcev, L.M. Robeson, M. Elimelech, B.D. Freeman. Maximizing the right stuff: The trade-off between membrane permeability and selectivity. Science 2017, 356 (6343):eaab0530.
17. G.M. Geise, H.B. Park, A. C. Sagle, B. D. Freeman, J. E. McGrath. Water permeability and water/salt selectivity tradeoff in polymers for desalination. J. Membr. Sci. 2011, 369, 130-138.
18. J.R. Werber, A. Deshmukh, M. Elimelech. The critical need for increased selectivity, not increased water permeability, for desalination membranes. Environ. Sci. Technol. Lett. 2016, 3, 112-120.
19. Z.C. Ng, W.J. Lau, T. Matsuura, A.F. Ismail. Thin film nanocomposite RO membranes: Review on fabrication techniques and impacts of nanofiller characteristics on membrane properties. Chem. Eng. Res. Des. 2021, 165, 81-105.

20. C. Zhang, B-H. Wu, M.Q. Ma, Z. Wang, Z-K. Xu. Ultrathin metal/covalent–organic framework membranes towards ultimate separation. Chem. Soc. Rev. 2019, 48, 3811-3841.
21. W.J. Koros. Evolving beyond the thermal age of separation processes: membranes can lead the way. AIChE J. 2004, 50, 2326.
22. MT. M, Pendergast, E.M.V Hoek. A review of water treatment membrane nanotechnologies. Energy Environ. Sci., 2011, 4,1946-1971.
23. A. Hospital, J.R. Goñi, M. Orozco, J. Gelpi. Molecular dynamics simulations: advances and applications. Adv Appl. Bioinform. Chem. 2015,8,37-47.
24. T. Humplik, J. Lee, S. O'hern, B. Fellman, M. Baig, S. Hassan, M. Atieh, F. Rahman, T. Laoui, R. Karnik, E.N. Wang. Nanostructured materials for water desalination. Nanotechnology 2011, 22, 292001.
25. F.-Y. Zhao, Y.-L. Ji, X.-D. Weng, Y.-F. Mi, C.-C. Ye, Q.-F. An, C.-J. Gao. High-flux positively charged nanocomposite nanofiltration membranes filled with poly (dopamine) modified multiwall carbon nanotubes. ACS Appl. Mater. Interfaces 2016, 8, 6693−6700.
26. C. Zhang, K. Wei, W. Zhang, Y. Bai, Y. Sun, J. Gu. Graphene oxide quantum dots incorporated into a thin film nanocomposite membrane with high flux and antifouling properties for low-pressure nanofiltration. ACS Appl. Mater. Interfaces 2017, 9, 11082−11094.
27. X. Song, R.S. Zambare, S. Qi, B. N. Sowrirajalu, A. P. James Selvaraj, C. Y. Tang, C. Gao. Charge-Gated Ion Transport through Polyelectrolyte Intercalated Amine Reduced Graphene Oxide Membranes. ACS Appl. Mater. Interfaces 2017, 9, 41482−41495.
28. B. Chen, H. Jiang, X. Liu, X. Hu. Molecular insight into water desalination across multilayer graphene oxide membranes. ACS Appl. Mater. Interfaces 2017, 9, 22826−22836.
29. C. Tang, Z. Wang, I. Petrinić, A. G. Fane, C. Hélix-Nielsen. Biomimetic aquaporin membranes coming of age. Desalination 2015, 368, 89−105.
30. R. Mahajan, R. Burns, M. Schaeffer, W. J. Koros. Challenges in forming successful mixed matrix membranes with rigid polymeric materials. J. Appl. Polym. Sci. 2002, 86, 881–890.
31. W. Lei, D. Portehault, D. Liu, S. Qin, Y. Chen. Porous boron nitride nanosheets for effective water cleaning. Nat. Commun. 2013, 4, 1777.

32. W. Hirunpinyopas, E. Prestat, S. D. Worrall, S. J. Haigh, R. A. W. Dryfe, M. A. Bissett. Desalination and Nanofiltration through Functionalized Laminar MoS2 Membranes. ACS Nano 2017, 11, 11082-11090.
33. X. Liu, N. K. Demir, Z. Wu, K. Li. Highly Water-Stable Zirconium Metal−Organic Framework UiO-66 Membranes Supported on Alumina Hollow Fibers for Desalination. J. Am. Chem. Soc. 2015, 137, 6999−7002.
34. S. Cong, Y. Yuan, J. Wang, Z. Wang, F. Kapteijn, X. Liu. Highly Water-Permeable Metal-Organic Framework MOF-303 Membranes for Desalination. J. Am. Chem. Soc. 2021, 143, 20055-20058.
35. R. Wang, M. Wei, Y. Wang. Secondary growth of covalent organic frameworks (COFs) on porous substrates for fast desalination. J. Membr. Sci. 2020, 604,118090.
36. X. Li, S. Chou, R. Wang, L. Shi, W. Fang, G. Chaitra, C. Y. Tang, J. Torres, X. Hu, A. G. Fane. Nature gives the best solution for desalination: Aquaporin-based hollow fiber composite membrane with superior performance. J. Membr. Sci. 2015, 494, 68–77.
37. C.-Y. Chong, W.-J. Lau, N. Yusof, G.-S. Lai, A.F. Ismail. Roles of nanomaterial structure and surface coating on thin film nanocomposite membranes for enhanced desalination. Compos. B Eng. 2019, 160, 471–479.
38. D. Emadzadeh, W.J. Lau, M. Rahbari-Sisakht, A. Daneshfar, M. Ghanbari, A. Mayahi, T. Matsuura, A.F. Ismail. A novel thin film nanocomposite reverse osmosis membrane with superior anti-organic fouling affinity for water desalination. Desalination 2015, 368, 106–113.
39. L. He, L.F. Dumée, C. Feng, L. Velleman, R. Reis, F. She, W. Gao, L. Kong. Promoted water transport across graphene oxide–poly (amide) thin film composite membranes and their antibacterial activity. Desalination 2015, 365, 126-135.
40. F. Asempour, S. Akbari, D. Bai, D. Emadzadeh, T. Matsuura, B. Kruczek. Improvement of stability and performance of functionalized halloysite nano tubes-based thin film nanocomposite membranes. J. Membr. Sci. 2018, 563, 470–480.
41. V. Vatanpour, M. Safarpour, A. Khataee, H. Zarrabi, M.E. Yekavalangi, M. Kavian. A thin film nanocomposite reverse osmosis membrane containing amine-functionalized carbon nanotubes. Sep. Purif. Technol. 2017, 184, 135–143.
42. L. Zhang, G.Z. Shi, S. Qiu, L.H. Cheng, H.L. Chen. Preparation of high-flux thin film nanocomposite reverse osmosis membranes by incorporating functionalized multi-walled carbon nanotubes. Desalin. Water Treat. 2011, 34,19–24.

43. H. Zhao, S. Qiu, L. Wu, L. Zhang, H. Chen, C. Gao. Improving the performance of polyamide reverse osmosis membrane by incorporation of modified multi-walled carbon nanotubes. J. Membr. Sci. 2014, 450, 249–256.
44. Z. Ng, C. Chong, W. Lau, M. Karaman, A.F. Ismail. Boron removal and antifouling properties of thin-film nanocomposite membrane incorporating PECVD-modified titanate nanotubes. J. Chem. Technol. Biotechnol. 2019, 94,2772–2782.
45. M. Zargar, Y. Hartanto, B. Jin, S. Dai.Polyethylenimine modified silica nanoparticles enhance interfacial interactions and desalination performance of thin film nanocomposite membranes. J. Membr. Sci. 2017, 541, 19–28.
46. N. Akther, Z.Yuan, Y.Chen, S.Lim, S.Phuntsho, N.Ghaffour, H.Matsuyama, H. Shon. Influence of graphene oxide lateral size on the properties and performances of forward osmosis membrane. Desalination 2020, 484, 114421.
47. W. J. Lau, S. Gray, T. Matsuura, D. Emadzadeh, J. Paul Chen, A.F. Ismail. A review on polyamide thin film nanocomposite (TFN) membranes: history, applications, challenges and approaches. Water Res. 2015, 80, 306–324.
48. T.H. Lee, J.Y. Oh, S.P. Hong, J.M. Lee, S.M. Roh, S.H. Kim, H.B. Park. ZIF-8 particle size effects on reverse osmosis performance of polyamide thin-film nanocomposite membranes: importance of particle deposition. J. Membr. Sci. 2019, 570–571, 23–33.
49. F. Asempour, S. Akbari, D. Bai, D. Emadzadeh, T. Matsuura, B. Kruczek. Improvement of stability and performance of functionalized halloysite nano tubes-based thin film nanocomposite membranes. J. Membr. Sci. 2018, 563, 470–480.
50. G. N. B. Baroña, J. Lim, M. Choi, B. Jung. Interfacial polymerization of polyamide-aluminosilicate SWNT nanocomposite membranes for reverse osmosis. Desalination 2013, 325, 138e147.
51. X. Song, Q. Zhou, T. Zhang, H. Xu, Z. Wang. Pressure-assisted preparation of graphene oxide quantum dot-incorporated reverse osmosis membranes: antifouling and chlorine resistance potentials. J. Mater. Chem. A 2016, 4, 16896–16905
52. X. Gao, Y. Li, X. Yang, Y. Shang, Y. Wang, B. Gao, Z. Wang. Highly permeable and antifouling reverse osmosis membranes with acidified graphitic carbon nitride nanosheets as nanofillers. J. Mater. Chem. A 2017, 5, 19875–19883.
53. S.G. Kim, J.H. Chun, B.H. Chun, S.H. Kim. Preparation, characterization and performance of poly (aylene ether sulfone)/modified silica nanocomposite reverse osmosis membrane for seawater desalination. Desalination 2013, 325, 76–83.

54. C. Xu, F. Shao, Z. Yi, H. Dong, Q. Zhang, J. Yu, J. Feng, X. Wu, Q. Zhang, L. Yu, L. Dong. Highly chlorine resistance polyamide reverse osmosis membranes with oxidized graphitic carbon nitride by ontology doping method. Sep. Purif. Technol. 2019, 223, 178–185.
55. M.E.A. Ali, L. Wang, X. Wang, X. Feng. Thin film composite membranes embedded with graphene oxide for water desalination. Desalination 2016, 386, 67–76.
56. D. Emadzadeh, M. Ghanbari, W.J. Lau, M. Rahbari-Sisakht, D. Rana, T. Matsuura, B. Kruczek, A.F. Ismail. Surface modification of thin film composite membrane by nanoporous titanate nanoparticles for improving combined organic and inorganic antifouling properties. Mater. Sci. Eng. C 2017, 75, 463–470.
57. H. J. Kim, M.-Y. Lim, K.H. Jung, D.-G. Kim, J.-C. Lee. High-performance reverse osmosis nanocomposite membranes containing the mixture of carbon nanotubes and graphene oxides. J. Mater. Chem. A 2015, 3, 6798–6809.
58. M. Ghanbari, D. Emadzadeh, W.J. Lau, T. Matsuura, A.F. Ismail. Synthesis and characterization of novel thin filmnanocomposite reverse osmosis membranes with improvedorganic fouling properties for water desalination. RSC Adv. 2015, 5, 21268–21276.
59. A. Inurria, P. Cay-Durgun, D. Rice, H. Zhang, D.-K. Seo, M. L. Lind, F. Perreault. Polyamide thin-film nanocompositemembranes with graphene oxide nanosheets: balancingmembrane performance and fouling propensity. Desalination 2019, 451, 139–147.
60. M. Kadhom, B. Deng. Thin film nanocompositemembranes filled with bentonite nanoparticles for brackishwater desalination: a novel water uptake concept. Microporous Mesoporous Mater., 2019, 279, 82–91.
61. H. D. Lee, H. W. Kim, Y.H. Cho, H. B. Park. Experimental Evidence of Rapid Water Transport through Carbon Nanotubes Embedded in Polymeric Desalination Membranes. Small 2014, 10, 2653–2660.
62. S. Roy, S.A. Ntim, S. Mitra, K. K. Sirkar. Facile Fabrication of Superior Nanofiltration Membranes from Interfacially Polymerized CNT-Polymer Composites. J. Membr. Sci. 2011, 375, 81−87.
63. F. Zhao, Y. Ji, X. D. Weng, Y. Mi, C. Ye, Q. An, C. Gao. High flux Positively Charged Nanocomposite Nanofiltration Membranes Filled with Poly(dopamine) Modified Multiwall Carbon Nanotubes. ACS Appl. Mater. Interfaces 2016, 8, 6693−6700.

64. S. Casanova, T-Y. Liu, Y-M. J. Chew, A. Livingston, D. Mattia. High flux thin-film nanocomposites with embedded boron nitride nanotubes for nanofiltration. J. Membr. Sci. 2020, 597,117749.
65. S. Abdikheibari, W. Lei, L. F. Dumée, A. J. Barlow, K. Baskaran. Novel thin film nanocomposite membranes decorated with few-layered boron nitride nanosheets for simultaneously enhanced water flux and organic fouling resistance. Appl. Surf. Sci., 2019, 488, 565-577.
66. X. Wang, Y. Zhao, E. Tian, J. Li, Y. Ren. Graphene Oxide-Based Polymeric Membranes for Water Treatment. Adv. Mater. Interfaces 2018, 5, 1701427−1701427.
67. S. Bano, A. Mahmood, S.J. Kim, K.H. Lee. Graphene Oxide Modified Polyamide Nanofiltration Membrane with Improved Flux and Antifouling Properties. J. Mater. Chem. A 2015, 3, 2065−2071.
68. Y. Zhang, H. Ruan, C. Guo, J. Liao, J. Shen, C. Gao. Thin-Film Nanocomposite Reverse Osmosis Membranes with Enhanced Antibacterial Resistance by Incorporating p-Aminophenol-Modified Graphene Oxide. Sep. Purif. Technol. 2020, 234, 116017.
69. Y. Kang, M. Obaid, J. Jang, I.S. Kim. Sulfonated Graphene Oxide Incorporated Thin Film Nanocomposite Nanofiltration Membrane to Enhance Permeation and Antifouling Properties. Desalination 2019, 470, 114125−114136.
70. W. Ma, T. Chen, S. Nanni, L. Yang, Z. Ye, M.S. Rahaman. Zwitterion-Functionalized Graphene Oxide Incorporated Polyamide Membranes with Improved Antifouling Properties. Langmuir 2019, 35, 1513−1525.
71. G. Eda, H. Yamaguchi, D. Voiry, T. Fujita, M. Chen, M. Chhowalla. Photoluminescence from chemically exfoliated MoS2. Nano Lett. 2011, 11, 5111.
72. A. Splendiani, L. Sun, Y. Zhang, T. Li, J. Kim, C.-Y. Chim, G. Galli, F. Wang. Emerging photoluminescence in monolayer MoS2. Nano Lett. 2010, 10, 1271.
73. Z. Wang, Q. Tu, S. Zheng, J. J. Urban, S. Li, B. Mi. Understanding the Aqueous Stability and Filtration Capability of MoS2 Membranes. Nano Lett. 2017,17, 7289-7298.
74. Y. Li, S. Yang, K. Zhang, B. Van der Bruggen. Thin film nanocomposite reverse osmosis membrane modified by two dimensional laminar MoS2 with improved desalination performance and fouling-resistant characteristics. Desalination 2019, 454, 48-58.
75. X. Li, Y. Liu, J. Wang, J. Gascon, J. Li, B. V. Bruggen. Metal Organic Frameworks Based Membranes for Liquid Separation. Chem. Soc. Rev. 2017, 46, 7124−7144.

76. Z. Liao, X. Fang, J. Xie, Q. Li, D. Wang, X. Sun, L. Wang, J. Li. Hydrophilic Hollow Nanocube Functionalized Thin Film Nanocomposite Membrane with Enhanced Nanofiltration Performance. ACS Appl. Mater. Interfaces 2019, 11, 5344−5352.
77. X. Zhang, Y. Zhang, T. Wang, Z. Fan, G. Zhang. A Thin Film Nanocomposite Membrane with Preimmobilized UiO-66-NH2 Toward Enhanced Nanofiltration Performance. RSC Adv. 2019, 9, 24802−24810.
78. R. Wang, X. Shi, A. Xiao, W. Zhou, Y. Wang. Interfacial polymerization of covalent organic frameworks (COFs) on polymeric substrates for molecular separations. J. Membr. Sci. 2018, 566,197-204.
79. W. Zhou, M. Wei, X. Zhang, F. Xu, Y. Wang. Fast Desalination by Multilayered Covalent Organic Framework (COF) Nanosheets. ACS Appl. Mater. Interfaces 2019, 11, 16847-16854.
80. M. J. C. Ordoñez, K.J. Balkus, J. P. Ferraris, I. H. Musselman. Molecular sieving realized with ZIF-8/ Matrimidâ mixed-matrix membranes. J. Membr. Sci. 2010, 361, 28–37.
81. K. M. Gupta, Z. Qiao, K. Zhang, J. Jiang. Seawater pervaporation through zeolitic imidazolate framework membranes: Atomistic simulation study. ACS Appl. Mater. Interfaces 2016, 8, 13392–13399.
82. H. Zhang, J. Hou, Y. Hu, P. Wang, R. Ou, L. Jiang, J. Z. Liu, B. D. Freeman, A. J. Hill, H. Wang. Ultrafast selective transport of alkali metal ions in metal organic frameworks with subnanometer pores. Sci. Adv. 2018, 4, eaaq0066.
83. S. Chen, C. Zhu, W. Xian, X. Liu, X-L. Liu, Q. Zhang, S. Ma, Q. Sun. Imparting Ion Selectivity to Covalent Organic Framework Membranes Using de Novo Assembly for Blue Energy Harvesting. J. Am. Chem. Soc. 2021, 143, 9415-9422.
84. H. Fan, M. Peng, I. Strauss, A. Mundstock, H. Meng, J. Caro. MOF-in-COF molecular sieving membrane for selective hydrogen separation. Nat. Commun. 2021, 12, 38.
85. M. Firoozi, Z. Rafiee, K. Dashtian. New MOF/COF Hybrid as a Robust Adsorbent for Simultaneous Removal of Auramine O and Rhodamine B Dyes. ACS Omega 2020,5, 9420-9428.
86. F.-M. Zhang, J.-L. Sheng, Z.-D. Yang, X.-J. Sun, H.-L. Tang, M. Lu, H. Dong, F.-C. Shen, J. Liu, Y.-Q. Lan. Rational design of MOF/COF hybrid materials for photocatalytic H2 evolution in the presence of sacrificial electron donors. Angew. Chem. Int. Ed. 2018, 57, 12106−12110.

87. Y. Cheng, Y. Ying, L. Zhai, G. Liu, J. Dong, Y. Wang, M. P. Christopher, S. Long, Y. Wang, D. Zhao. Mixed matrix membranes containing MOF@COF hybrid fillers for efficient CO2/ CH4 separation. J. Membr. Sci. 2019, 573, 97−106.
88. Y.Yan, T. He, B. Zhao, K. Qi, H. Liu, B. Y. Xia. Metal/ covalent-organic frameworks-based electrocatalysts for water splitting. J. Mater. Chem. A 2018, 6, 15905.
89. J. Fu, S. Das, G. Xing, T. Ben, V. Valtchev, S. Qiu. Fabrication of COF-MOF Composite Membranes and Their Highly Selective Separation of H2/CO2. J. Am. Chem. Soc. 2016, 138, 7673-7680.
90. P. Agre. Aquaporin water channels (Nobel Lecture). Angew. Chem. Int. Ed. Engl. 2004, 43, 4278–4290.
91. C. J. Porter, J. R. Werber, M. Zhong, C.J. Wilson, M. Elimelech. Pathways and Challenges for Biomimetic Desalination Membranes with Sub-Nanometer Channels. ACS Nano 2020,14,10894-10916.
92. Y.Kaufman, A.Berman,V. Freger. Supported lipid bilayer membranes for water purification by reverse osmosis. Langmuir 2010, 26,7388–7395.
93. X. Li, R.Wang, C.Tang, A.Vararattanavech, Y.Zhao, J.Torres, T.Fane. Preparation of supported lipid membranes for aquaporin Z incorporation. Coll. Surf. B:Biointerfaces 2012, 94, 333–340.
94. H. Wang, T.-S. Chung, Y.W. Tong, K. Jeyaseelan, A. Armugam, Z. Chen, M. Hong, W.Meier. Highly permeable and selective pore-spanning biomimetic membrane embedded with aquaporin Z. Small 2012, 8, 1185–1190.
95. P.S. Zhong, T.-S. Chung, K. Jeyaseelan, A.Armugam. Aquaporin-embedded biomimetic membranes for nanofiltration. J. Membr. Sci. 2012, 407–408, 27–33.
96. P.H.H. Duong, T.-S. Chung, K. Jeyaseelan, A.Armugam, Z.Chen, J.Yang, M. Hong. Planar biomimetic aquaporin-incorporated triblock copolymer membranes on porous alumina supports for nanofiltration. J.Memb.Sci. 2012, 409–410, 34–43.
97. A. Striolo, A. Michaelides, L. Joly. The Carbon-Water Interface: Modeling Challenges and Opportunities for the Water-Energy Nexus. Annu. Rev. Chem. Biomol. Eng. 2016, 7, 533.
98. J. H. Walther, K. Ritos, E. R. Cruz-Chu, C. M. Megaridis,P. Koumoutsakos. Barriers to superfast water transport in carbon nanotube membranes. Nano Lett. 2013, 13, 1910.
99. S. Riniker, Fixed-Charge Atomistic Force Fields for Molecular Dynamics Simulations in the Condensed Phase: An Overview. J. Chem. Inf. Model. 2018, 58, 565–578.

100. L. Monticelli, D. P. Tieleman. Force Fields for Classical Molecular Dynamics. Methods Mol. Biol. 2013, 924, 197–213.
101. H. Fang, H. Demir, P. Kamakoti, D. S. Sholl. Recent developments in first-principles force fields for molecules in nanoporous materials. J. Mater. Chem. A 2014, 2, 274-291.
102. G. Hummer, J. C. Rasaiah, J. P. Noworyta. Water conduction through the hydrophobic channel of a carbon nanotube. Nature 2001, 414, 188–190.
103. T. Werder, J. Walther, R. Jaffe, T. Halicioglu, P. Koumoutsakos. On the Water-carbon Interaction for Use in Molecular Dynamics Simulations of Graphite and Carbon Nanotubes. J. Phys. Chem. B 2003, 107, 1345–1352.
104. S. Joseph, N. R. Aluru. Why Are Carbon Nanotubes Fast Transporters of Water?. Nano Lett. 2008, 8, 452–458.
105. K. V. Prasad, S. K. Kannam, R. Hartkamp, S. P. Sathian. Water desalination using graphene nanopores: influence of the water models used in simulations. Phys. Chem. Chem. Phys. 2018, 20, 16005–16011.
106. M. Heiranian, A. B. Farimani, N. R. Aluru.Water Desalination with a Single-layer MoS2 Nanopore. Nat. Commun. 2015, 6, 8616.
107. K. M. Gupta, J. Jiang. Water Desalination through a Zeolitic Imidazolate Framework Membrane by Electro- and Thermo-Osmosis: Which Could Be More Efficient?. ChemistrySelect 2017, 2, 3981–3986.
108. K. M. Gupta, K Zhang, J. Jiang. Efficient Removal of Pb2+ from Aqueous Solution by an Ionic Covalent–Organic Framework: Molecular Simulation Study. Ind. Eng. Chem. Res. 2018, 57, 6477-6482.
109. A. K. Rappe, C. J. Casewit, K. S. Colwell, W. A. Goddard, W. M. Skiff. UFF, a full periodic table force field for molecular mechanics and molecular dynamics simulations. J. Am. Chem. Soc., 1992, 114, 10024.
110. S. L. Mayo, B. D. Olafson, W. A. Goddard. DREIDING: a generic force field for molecular simulations. J. Phys. Chem., 1990, 94, 8897.
111. W. L. Jorgensen, D. S. Maxwell, J. TiradoRives. Development and Testing of the OPLS All-Atom Force Field on Conformational Energetics and Properties of Organic Liquids. J. Am. Chem. Soc., 1996, 118, 11225.
112. H. J. C. Berendsen, J. R. Grigera, T. P. Straatsma. The missing term in effective pair potentials. J. Phys. Chem. 1987, 91, 6269-6271.

113. W. L. Jorgensen, J. Chandrasekhar, J. D. Madura, R. W. Impey, M. L. Klein. Comparison of simple potential functions for simulating liquid water. J. Chem. Phys., 1983, 79, 926-935.
114. J. L. F. Abascal, C. Vega. A general purpose model for the condensed phases of water: TIP4P/2005. J. Chem. Phys. 2005, 123, 234505.
115. M. Shahbabaei, D. Kim. Advances in nanofluidics for water purification and filtration: molecular dynamics (MD) perspective. Environ. Sci.: Nano 2021, 8,2120-2151.
116. M.P. Allen. Computational soft matter: from synthetic polymers to proteins lecture notes, Introduction to Molecular Dynamics Simulation, John von Neumann Institute for Computing, Jülich, Germany, 2004.
117. L.A. Richards, A.I. Schafer, B.S. Richards, B. Corry. The importance of dehydration in determining ion transport in narrow pores. Small 2012, 8, 1701-1709.
118. L.Y. Wang, R.S. Dumont, J.M. Dickson. Nonequilibrium molecular dynamics simulation of water transport through carbon nanotube membranes at low pressure. J. Chem. Phys. 2012, 137, 044102.
119. A. Kalra, S. Garde, G. Hummer. Osmotic water transport through carbon nanotube membranes. Proc. Natl. Acad. Sci., 2003,100, 10175-10180.
120. W.J. Koros, G.K. Fleming. Membrane-based gas separation. J. Membr. Sci. 1993, 83,1-80.
121. F. Zhu, E. Tajkhorshid, K. Schulten. Pressure-Induced Water Transport in Membrane Channels Studied by Molecular Dynamics. Biophys. J. 2002, 83, 154–160.
122. G. S. Heffelfinger, F. V. Swol. Diffusion in Lennard-Jones fluids using dual control volume grand canonical molecular dynamics simulation (DCV-GCMD). J. Chem. Phys. 1994, 100, 7548.
123. L. Wang, R. S. Dumont and J. M. Dickson. Molecular dynamic simulations of pressure-driven water transport through polyamide nanofiltration membranes at different membrane densities. RSC Adv. 2016, 6, 63586–63596.
124. M. Shen, S. Keten, R. M. Lueptow. Dynamics of water and solute transport in polymeric reverse osmosis membranes via molecular dynamics simulations. J. Membr. Sci. 2016, 506, 95–108.
125. Z. Hu, Y. Chen, J. Jiang. Zeolitic imidazolate framework-8 as a reverse osmosis membrane for water desalination: Insight from molecular simulation. J. Chem. Phys. 2011, 134, 134705.

126. K. M. Gupta, K. Zhang, J. Jiang. Water desalination through zeolitic imidazolate framework membranes: significant role of functional groups. Langmuir 2015, 31,13230–13237.

127. A. Ozcan, C. Perego, M. Salvalaglio, M. Parrinello, O. Yazaydin. Concentration gradient driven molecular dynamics: a new method for simulations of membrane permeation and separation. Chem. Sci. 2017,8, 3858-3865.

128. F. A. Cabrales-Navarro, J. L. G´omez-Ballesteros, P. B. Balbuena. Molecular dynamics simulations of metal-organic frameworks as membranes for gas mixtures separation. J. Membr. Sci. 2013, 428, 241–250.

129. M. Ding, A. Szymczyk and A. Ghoufi. Hydration of a polyamide reverse-osmosis membrane. Desalination 2015, 368, 76–80.

130. Z. Hat´o, A. Kaviczki and T. Kristof. A simple method for the simulation of steady-state diffusion through membranes: pressure-tuned, boundary-driven molecular dynamics. Mol. Simul 2015, 42, 71– 80.

131. P. I. Pohl, G. S. Heffelfinger. Massively parallel molecular dynamics simulation of gas permeation across porous silica membranes. J. Membr. Sci. 1999, 155, 1–7.

132. R. F. Cracknell, D. Nicholson, N. Quirke. Direct molecular dynamics simulation of flow down a chemical potential gradient in a slit-shaped micropore. Phys. Rev. Lett. 1995, 74, 2463–2466.

133. L. Xu, M. G. Sedigh, M. Sahimi, T. T. Tsotsis. Nonequilibrium Molecular Dynamics Simulation of Transport of Gas Mixtures in Nanopores. Phys. Rev. Lett. 1998, 80, 3511–3514.

134. F.Q. Zhu, E. Tajkhorshid, K. Schulten. Theory and simulation of water permeation in Aquaporin-1. Biophys. J. 2004, 86, 50-57.

135. A. Mollahosseini, A. Abdelrasoul. Molecular dynamics simulation for membrane separation and porous materials: A current state of art review. J. Mol. Graph. Model. 2021, 107,107947.

136. X. Zhang, M. Wei, F. Xu, Y. Wang. Pressure-Dependent Ion Rejection in Nanopores. J. Phys. Chem. C 2020 124, 20498-20505

137. L. Zhang, L. Jia, J. Zhang, J. Li, L. Liang, Z. Kong, J-W. Shen, X. Wang, W. Zhang, H. Wang. Understanding the effect of chemical modification on water desalination in boron nitride nanotubes via molecular dynamics simulation. Desalination 2019, 464, 84-93 .

138. E.Y.M. Ang, T.Y. Ng, J. Yeo, R. Lin, K.R. Geethalakshmi. Nanoscale fluid mechanics working principles of transverse flow carbon nanotube membrane for enhanced desalination. Int. J. Appl. Mech. 2017, 09, 1750034.
139. C. Peter, G. Hummer. Ion Transport through Membrane-Spanning Nanopores Studied by Molecular Dynamics Simulations and Continuum Electrostatics Calculations. Biophys. J. 2005,89,2222-2234.
140. A. Striolo. The Mechanism of Water Diffusion in Narrow Carbon Nanotubes. Nano Lett. 2006, 6, 633-639.
141. D. Frenkel, B. Smith. Understanding Molecular Simulation: From Algorithms to Applications, Academic Press, San Diego, 2nd edn, 2002.
142. I. Medveď, R. Černý. Surface diffusion in porous media: A critical review. Microporous Mesoporous Mater., 2011,142, 405-422.
143. B. C. Bukowski, F.J. Keil, P.I. Ravikovitch, G. Sastre, R.Q. Snurr, M-O. Coppens. Connecting theory and simulation with experiment for the study of diffusion in nanoporous solids. Adsorption 2021, 27, 683-760.
144. T. Titze , A. Lauerer , L. Heinke , C. Chmelik , N. E. Zimmermann , F. J. Keil , D. M. Ruthven, J. Kärger. Transport in nanoporous materials including MOFs: the applicability of fick's laws. Angew. Chem. Int. Ed., 2015 , 54, 14580-14583.
145. H. Zhang, B. Liu, H.T. Kieu, M. S. Wu, K. Zhou, A.W-K. Law. Coarse-grained molecular dynamics study of membrane distillation through meso-size graphene channels. J. Membr. Sci., 2018, 558, 34-44.
146. J. Muscatello, E. A. Muller, A. A. Mostofi, A. P. Sutton. Multiscale molecular simulations of the formation and structure of polyamide membranes created by interfacial polymerization. J. Membr. Sci., 2017, 527, 180-190.
147. A. Ghoufi, A. Szymczyk. Computational Assessment of Water Desalination Performance of Multi-Walled Carbon Nanotubes. Adv. Theory Simul. 2020, 3, 900254.
148. H. Gao, Q. Shi, D. Rao, Y. Zhang, J. Su, Y. Liu, Y. Wang, K. Deng, R. Lu. Rational Design and Strain Engineering of Nanoporous Boron Nitride Nanosheet Membranes for Water Desalination. J. Phys. Chem. C 2017, 121, 22105-22113.
149. M. Shahbabaei, D. Kim. Exploring fast water permeation through aquaporin-mimicking membranes. Phys. Chem. Chem. Phys., 2020, 22, 1333-1348.
150. D. Cohen-Tanugi, J. C. Grossman. Water Desalination across Nanoporous Graphene. Nano Lett., 2012, 12, 3602–3608.

151. Cao, V. Liu, A. Barati Farimani. Water Desalination with Two-Dimensional Metal–Organic Framework Membranes. Nano Lett., 2019, 19, 8638-8643.
152. K. Zhang, Z. He, K. M. Gupta, J. Jiang. Computational design of 2D functional covalent– organic framework membranes for water desalination. Environ. Sci.: Water Res. Technol., 2017, 3, 735–743.
153. B. Corry. Designing Carbon Nanotube Membranes for Efficient Water Desalination. J. Phys. Chem. B 2008, 112, 1427-1434.
154. M. Thomas, B. Corry. A computational assessment of the permeability and salt rejection of carbon nanotube membranes and their application to water desalination. Phil. Trans. R. Soc. A 2016, 374, 20150020.
155. M. E. Suk, A. V. Raghunathan, N. R. Aluru. Fast reverse osmosis using boron nitride and carbon nanotubes. Appl. Phys. Lett., 2008, 92, 133120.
156. C. Y. Won, N. R. Aluru. Water Permeation through a Subnanometer Boron Nitride Nanotube. J. Am. Chem. Soc., 2007, 129, 2748−2749.
157. L. Zhang, L. Jia, J. Zhang, J. Li, L. Liang, Z. Kong, J-W. Shen, X. Wang, W. Zhang, H. Wang. Understanding the effect of chemical modification on water desalination in boron nitride nanotubes via molecular dynamics simulation. Desalination 2019, 464, 84-93 .
158. Q. Li, D. Yang, J. Shi, X. Xu, S. Yan, Q. Liu. Biomimetic modification of large diameter carbon nanotubes and the desalination behavior of its reverse osmosis membrane. Desalination 2016, 379,164−171.
159. J. Zheng, E.M. Lennon, H.K. Tsao, Y.J. Sheng, S. Jiang. Transport of a liquid water and methanol mixture through carbon nanotubes under a chemical potential gradient. J. Chem. Phys., 2005, 122, 214702.
160. S. Joseph, R. J. Mashl, E. Jakobsson, N. R. Aluru. Electrolytic Transport in Modified Carbon Nanotubes. Nano Lett., 2003, 3, 1399–1403.
161. Y. Hong, J. Zhang, C. Zhu, X. C. Zeng, J. S. Francisco. Water desalination through rim functionalized carbon nanotubes. J. Mater. Chem. A 2019,7, 3583-3591
162. E.Y.M. Ang, T.Y. Ng, J. Yeo, R. Lin, Z. Liu, K.R. Geethalakshmi. Carbon nanotube arrays as multilayer transverse flow carbon nanotube membrane for efficient desalination. J. Membr. Sci., 2019, 581,383-392.
163. S. Gravelle, L. Joly, F. Detcheverry, C. Ybert, C. Cottin-Bizonne,L. Bocquet. Optimizing water permeability through the hourglass shape of aquaporins. Proc. Nat. Acad. Sci., 2013, 110, 16367–16372.

164. S. Gravelle, L. Joly, C. Ybert, L. Bocquet. Large permeabilities of hourglass nanopores: From hydrodynamics to single file transport. J. Chem. Phys., 2014, 141, 18C526.

165. D. Tang, D. Kim. Study on the transport of water molecules under the geometry confinement of aquaporin like nanopores. Appl. Therm. Eng., 2014, 72, 120–125.

166. D. Tang, L. Li, M. Shahbabaei, Y. E. Yoo, D. Kim, Molecular Dynamics Simulation of the Effect of Angle Variation on Water Permeability through Hourglass-Shaped Nanopores. Materials 2015, 8, 7257–7268.

167. C. Han, D. Tang, D. Kim, Molecular dynamics simulation on the effect of pore hydrophobicity on water transport through aquaporin-mimic nanopores. Colloids Surf. A 2015, 481, 38–42.

168. M. Shahbabaei, D. Kim. Effect of hourglass-shaped nanopore length on osmotic water transport. Chem. Phys., 2016, 477, 24–31.

169. M. Shahbabaei, D. Kim. Molecular dynamics simulation of transport characteristics of water molecules through high aspect ratio hourglass-shaped pore. Colloids Surf. A 2016, 507, 190–199.

170. A. Nalaparaju, J. Wang, J. Jiang. Water Permeation through Conical Nanopores: Complex Interplay between Surface Roughness and Chemistry. Adv. Theory Simul., 2020, 3, 2000025.

171. X. Zhang, W. Zhou, F. Xu, M. Wei, Y. Wang. Resistance of water transport in carbon nanotube membranes. Nanoscale 2018, 10, 13242.

172. M. Shahbabaei, D. Tang, D. Kim, Simulation Insight into Water Transport Mechanisms through Multilayer Graphene-based Membrane. Comput. Mater. Sci., 2017, 128, 87–97.

173. M. Shahbabaei, D. Kim. Molecular Dynamics Simulation of Water Transport Mechanisms through Nanoporous Boron Nitride and Graphene Multilayers. J. Phys. Chem. B 2017, 121, 4137–4144.

174. M. Shahbabaei, D. Kim, Transport of water molecules through noncylindrical pores in multilayer nanoporous graphene. Phys. Chem. Chem. Phys., 2017, 19, 20749–20759.

175. M. Razmkhah, A. Ahmadpour, M.T.H. Mosavian, F. Moosavi. What is the effect of carbon nanotube shape on desalination process? A simulation approach. Desalination 2017, 407, 103.

176. W. Li, W. Wang, Y. Zhang, Y. Yan, P. Kr´al, J. Zhang. Highly efficient water desalination in carbon nanocones. Carbon 2018, 129, 374.

177. V. P. Kurupath, S. K. Kannam, R. Hartkamp, S. P. Sathian. Highly efficient water desalination through hourglass shaped carbon nanopores. Desalination 2021, 505,114978,
178. D. Konatham, J. Yu, T. A. Ho, A. Striolo. Simulation insights for graphene based water desalination membranes. Langmuir 2013, 29, 11884–11897.
179. K. Sint, B. Wang and P. Král. Selective Ion Passage through Functionalized Graphene Nanopores. J. Am. Chem. Soc., 2008, 130, 16448–16449.
180. A.K. Giri, F. Teixeira, M.N.D.S. Cordeiro. Salt separation from water using graphene oxide nanochannels: A molecular dynamics simulation study. Desalination 2019, 460, 1-14.
181. C. Fang, Z. Yu, R. Qiao. Impact of Surface Ionization on Water Transport and Salt Leakage through Graphene Oxide Membranes. J. Phys. Chem. C 2017,121, 13412-13420.
182. D. Cohen-Tanugi, L.C. Lin, J. C. Grossman. Multilayer nanoporous graphene membranes for water desalination. Nano Lett., 2016, 16, 1027–1033.
183. G. Hu, M. Mao, S. Ghosal. Ion transport through a graphene nanopore. Nanotechnology 2012, 23, 395501.
184. S. Zhao, J. Xue, W. Kang. Ion selection of charge-modified large nanopores in a graphene sheet. J. Chem. Phys., 2013, 139, 114702.
185. Y. Kang, Z. Zhang, H. Shi, J. Zhang, L. Liang, Q. Wang, H. Ågren, Y. Tu. Na^+ and K^+ ion selectivity by size-controlled biomimetic graphene nanopores. Nanoscale 2014, 6, 10666-10672.
186. J. Kou, J. Yao, L. Wu, X. Zhou, H. Lu, F. Wu, J. Fan. Nanoporous two-dimensional MoS2 membranes for fast saline solution purification. Phys. Chem. Chem. Phys., 2016, 18, 22210-22216.
187. P. O. Oviroh, T-C., Jen, J. Ren, L. M. Mohlala, R. Warmbier, S. Karimzadeh. Nanoporous MoS2 Membrane for Water Desalination: A Molecular Dynamics Study. Langmuir 2021 37, 7127-7137.
188. M. H. Köhler, J. R. Bordin, M.C. Barbosa. 2D nanoporous membrane for cation removal from water: Effects of ionic valence, membrane hydrophobicity, and pore size. J. Chem. Phys., 2018, 148, 222804.
189. J. Jiang. Recent development of in silico molecular modeling for gas and liquid separations in metal–organic frameworks. Curr. Opin. Chem. Eng., 2012, 1,138-144.
190. J. K. Holt, H. G. Park, Y. M. Wang, M. Stadermann, A. B. Artyukhin, C. P. Grigoropoulos, A. Noy, and O. Bakajin. Fast Mass Transport Through Sub-2-Nanometer Carbon Nanotubes. Science 2006, 312, 1034.

191. H. Bux, F. Y. Liang, Y. S. Li, J. Cravillon, M. Wiebcke, J. Caro. Zeolitic Imidazolate Framework Membrane with Molecular Sieving Properties by Microwave-Assisted Solvothermal Synthesis. J. Am. Chem. Soc., 2009, 131, 16000.

192. Y. Zhu, K. M. Gupta, Q. Liu, J. Jiang, J. Caro, A. Huang. Synthesis and seawater desalination of molecular sieving zeolitic imidazolate framework membranes. Desalination 2016, 385, 75-82.

193. E. Chen, L. Jia, C. Chen, F. Huang, L. Zhang. Understanding the transport mechanism of seawater through FMOF-1 and its derivative via molecular dynamics simulation. J. Mol. Liq., 2021, 325, 115209.

194. K.-S. Lin, A.K. Adhikari, C.-N. Ku, C.-L. Chiang, H. Kuo. Synthesis and characterization of porous HKUST-1 metal organic frameworks for hydrogen storage. Int. J. Hydrogen Energy 2012, 37, 13865-13871.

195. J. Canivet, A. Fateeva, Y. Guo, B. Coasne, D. Farrusseng. Water adsorption in MOFs: fundamentals and applications. Chem. Soc. Rev., 2014, 4, 5594–5617.

196. M. Dahanayaka, R. Babicheva, Z. Chen, A. W.-K. Law, M. S. Wu, K. Zhou. Atomistic simulation study of GO/HKUST-1 MOF membranes for seawater desalination via pervaporation. Appl. Surf. Sci., 2020, 503, 144198.

197. Y. Zhang, T. Fang, Q. Hou, Z. Li, Y. Yan. Water desalination of a new three-dimensional covalent organic framework: a molecular dynamics simulation study. Phys. Chem. Chem. Phys., 2020, 22,16978-16984.

198. F. Xu, L. Dai, Y. Wu, Z. Xu. Li^{+}/Mg^{2+} separation by membrane separation: The role of the compensatory effect. J. Membr. Sci., 2021, 636, 119542.

199. F. Xu, M. Wei, Y. Wang. Effect of hydrophilicity on ion rejection of sub-nanometer pores. Sep. Purif. Technol., 2021, 257, 117937.

200. T. Araki, R. Cruz-Silva, S. Tejima, K. Takeuchi, T. Hayashi, S. Inukai, T. Noguchi, A. Tanioka, T. Kawaguchi, M. Terrones, M. Endo. Molecular Dynamics Study of Carbon Nanotubes/Polyamide Reverse Osmosis Membranes: Polymerization, Structure, and Hydration. ACS Appl. Mater. Interfaces 2015, 7, 24566-24575.

201. T. Araki, R. Cruz-Silva, S. Tejima, J. Ortiz-Medina, A. Morelos-Gomez, K. Takeuchi, T. Hayashi, M. Terrones, M. Endo. Water Diffusion Mechanism in Carbon Nanotube and Polyamide Nanocomposite Reverse Osmosis Membranes: A Possible Percolation-Hopping Mechanism. Phys. Rev. Applied 2018, 9, 024018.

202. Q.-A. Gu, K. Li, S. Li, R. Cui, L. Liu, C. Yu, Y. Wang, Y. Zhou, G. Xiao. In silico study of structure and water dynamics in CNT/polyamide nanocomposite reverse osmosis membranes. Phys. Chem. Chem. Phys., 2020,22, 22324-22331.

203. Q. Li, K. Zhao, Q. Liu, J. Wang. Desalination behavior analysis of interior-modified carbon nanotubes doped membrane by dielectric spectrum and molecular simulation. Nanotechnology 2020, 31, 315705.

204. J.L. Fajardo-Diaz, A. Morelos-Gomez, R. Cruz-Silva, K. Ishii, T. Yasuike, T. Kawakatsu, A. Yamanaka, S. Tejima, K. Izu, S. Saito, J. Maeda, K. Takeuchi, M. Endo. Low-pressure reverse osmosis membrane made of cellulose nanofiber and carbon nanotube polyamide nano-nanocomposite for high purity water production. J. Chem. Eng., 2022, 448, 137359.

205. G. Wang, X. Zhang, M. Wei, Y. Wang. Mechanism of permeance enhancement in mixed-matrix reverse osmosis membranes incorporated with graphene and its oxides. Sep. Purif. Technol., 2021, 270,118818.

206. S. K. Salestan, S. F. Seyedpour, A. Rahimpour, A. A. Shamsabadi, A. Tiraferri, M. Soroush. Molecular Dynamics Insights into the Structural and Water Transport Properties of a Forward Osmosis Polyamide Thin-Film Nanocomposite Membrane Modified with Graphene Quantum Dots. Ind. Eng. Chem. Res., 2020, 59, 14447-14457.

207. N. Akther, Y. Kawabata, S. Lim, T. Yoshioka, S. Phuntsho, H. Matsuyama, H. K. Shon. Effect of graphene oxide quantum dots on the interfacial polymerization of a thin-film nanocomposite forward osmosis membrane: An experimental and molecular dynamics study. J. Membr. Sci., 2021, 630,119309.

208. Y. Song, M. Wei, F. Xu, Y. Wang. Transport mechanism of water molecules passing through polyamide/COF mixed matrix membranes. Phys.Chem.Chem.Phys., 2019, 21, 26591.

209. S. C. Solleder, D. Zengel, K. S. Wetzel, M. A. R. Meier. A scalable and high-yield strategy for the synthesis of sequence-defined macromolecules. Angew. Chem., Int. Ed., 2016, 55, 1204−1207.

210. J.-F. Lutz. Defining the field of sequence-controlled polymers. Macromol. Rapid Commun., 2017, 38, 1700582

211. H. Luo, K. Chang, K. Bahati, G. M. Geise. Engineering Selective Desalination Membranes via Molecular Control of Polymer Functional Groups. Environ. Sci. Technol. Lett., 2019, 6, 462-466.

212. J. Nambi Krishnan, K.R. Venkatachalam, O. Ghosh, K. Jhaveri, A. Palakodeti, N. Nair. Review of Thin Film Nanocomposite Membranes and Their Applications in Desalination. Front. Chem., 2020, 10,781372.

213. R. Rajakumaran, M. Kumar,R. Chetty. Morphological Effect of ZnO Nanostructures on Desalination Performance and Antibacterial Activity of Thin-Film Nanocomposite (TFN) Membrane. Desalination 2020, 495, 114673

214. W. Gai, D. L. Zhao, T.-S. Chung. Thin Film Nanocomposite Hollow Fiber Membranes Comprising Na+-Functionalized Carbon Quantum Dots for Brackish Water Desalination. Water Res., 2019, 154, 54–61.

215. Y. Wang, Z. Cao, A. Barati Farimani. Efficient water desalination with graphene nanopores obtained using artificial intelligence. npj 2D Mater. Appl., 2021, 5, 66.

216. Y. Wang, J. Wang, Z. Cao, A. Barati Farimani. Molecular Contrastive Learning of Representations via Graph Neural Networks. Nat. Mach. Intell., 2022, 4, 279–287.

217. M. Safarpour, V. Vatanpour, A. Khataee, H. Zarrabi, P. Gholami, M.E.Yekavalangi. High flux and fouling resistant reverse osmosis membrane modified with plasma treated natural zeolite. Desalination 2017, 411, 89–100.

218. N.A. Mahat, S.A. Shamsudin, N. Jullok, A.H. Ma'Radzi. Carbon quantum dots embedded polysulfone membranes for antibacterial performance in the process of forward osmosis. Desalination 2020, 493, 114618.

219. X.H. Ma, Z. Yang, Z.K. Yao, H. Guo, Z.L. Xu, C.Y. Tang. Interfacial polymerization with electrosprayed microdroplets: toward controllable and ultrathin polyamide membranes. Environ. Sci. Technol. Lett., 2018, 5, 117–122.

220. S. Yang, J. Wang, L. Fang, H. Lin, F. Liu, C.Y. Tang. Electrosprayed polyamide nanofiltration membrane with intercalated structure for controllable structure manipulation and enhanced separation performance. J. Membr. Sci., 2020, 602, 117971.

221. M.R. Chowdhury, J. Steffes, B.D. Huey, J.R. McCutcheon. 3D printed polyamide membranes for desalination. Science 2018, 361, 682–686.

222. T.H. Lee, I. Park, J.Y. Oh, J. K. Jang, H.B. Park. Facile preparation of polyamide thin-film nanocomposite membranes using spray-assisted nanofiller predeposition. Ind. Eng. Chem. Res., 2019, 58, 4248–4256.

223. W. Ma, A. Soroush, T. Van Anh Luong, G. Brennan, M.S. Rahaman, B. Asadishad, N. Tufenkji. Spray- and spin-assisted layer-by-layer assembly of copper nanoparticles on thin-film composite reverse osmosis membrane for biofouling mitigation. Water Res., 2016, 99, 188–199.